Bulletin of Mathematical Biology (2019) 81:3575–3622
https://doi.org/10.1007/s11538-018-0533-0

SPECIAL ISSUE: MATHEMATICS TO SUPPORT DRUG DISCOVERY AND DEVELOPMENT

Dynamics of Bone Cell Interactions and Differential Responses to PTH and Antibody-Based Therapies

Vincent Lemaire[1,2] · **David R. Cox**[1]

Received: 17 June 2017 / Accepted: 1 November 2018 / Published online: 20 November 2018

Abstract

We propose a mathematical model describing the dynamics of osteoblasts and osteoclasts in bone remodeling. The goal of this work is to develop an integrated modeling framework for bone remodeling and bone cell signaling dynamics that could be used to explore qualitatively combination treatments for osteoporosis in humans. The model has been calibrated using 57 checks from the literature. Specific global optimization methods based on qualitative objectives have been developed to perform the model calibration. We also added pharmacokinetics representations of three drugs to the model, which are teriparatide (PTH(1–34)), denosumab (a RANKL antibody) and romosozumab (a sclerostin antibody), achieving excellent goodness-of-fit of human clinical data. The model reproduces the paradoxical effects of PTH on the bone mass, where continuous administration of PTH results in bone loss but intermittent administration of PTH leads to bone gain, thus proposing an explanation of this phenomenon. We used the model to simulate different categories of osteoporosis. The main attributes of each disease are qualitatively well captured by the model, for example changes in bone turnover in the disease states. We explored dosing regimens for each disease based on the combination of denosumab and romosozumab, identifying adequate ratios and doses of both drugs for subpopulations of patients in function of categories of osteoporosis and the degree of severity of the disease.

Keywords Mathematical modeling · Bone remodeling · Wnt pathway · Intermittent PTH · Pharmacokinetics of monoclonal antibodies · Denosumab (anti-RANKL

In memory of David R. Cox.

David R. Cox: Deceased on January 21st, 2013.

Electronic supplementary material The online version of this article (https://doi.org/10.1007/s11538-018-0533-0) contains supplementary material, which is available to authorized users.

Extended author information available on the last page of the article

antibody) · Romosozumab (anti-sclerostin antibody) · Osteoporosis · Combination therapies

1 Introduction

In this paper, we present a reworked version of our previously published model describing the dynamics of bone cells (Lemaire et al. 2004). A major addition to the initial model originates from the discovery that some of the Wnt proteins have an overall promoting effect on the whole osteoblastic lineage (Daoussis and Andonopoulos 2011; Gogakos et al. 2009). This action is inhibited by sclerostin, a product of the SOST gene, which is mainly secreted by osteocytes and whose secretion is downregulated by PTH (Kramer et al. 2010; Paszty et al. 2010). We think that this new pathway, the Wnt-SOST pathway, could be the missing link explaining why PTH has different effect on bone mass when administrated continuously or intermittently (Gogakos et al. 2009). Testing this mechanism for the differential action of PTH was our initial motivation in proposing a new evolution of the model. We were also interested in testing human dosing of synthetic PTH(1–34), a RANKL antibody and a sclerostin antibody as mono or combination therapies. We therefore also included full pharmacokinetic descriptions of these three compounds. Other models of bone remodeling, which include sclerostin and a representation of the Wnt/SOST pathway, have been published recently (Eudy et al. 2015; Graham et al. 2013). However, they were developed with a different modeling focus and aimed at tackling different questions. The Graham et al. (2013) model, although based on biology, is relatively simple and was developed to perform theoretical exploration of the role of osteocytes in bone biology. The Eudy et al. (2015) model is a multi-scale physiological model initially designed to describe how osteocytes signals contribute to bone remodeling and how sclerostin antibodies can be used to harness these signals to maximize bone formation in patients with osteoporosis.

Our initial paper presents the biological introduction, mathematical formalism and assumptions of the model and discusses some therapeutic strategies (Lemaire et al. 2004). Here, we will focus on the development of the new evolution of the model. Just as in our earlier paper, the model we present here is a description of the localized process of bone remodeling. Although bone remodeling is a local process, it can also be modulated by systemic factors, such as hormones, like estrogen or vitamin D, calcium homeostasis, as well as by mechanical inputs. These systemic regulators are not directly represented in the model. While we believe the model predictions regarding the local bone milieu are validated and solid, the interpretation of these predictions at a wider systemic level should be considered with caution if quantitative precision is needed. On that matter, the model should be regarded as a tool for qualitative exploration. We start, in Sect. 2, by presenting the structure of the model and the biological literature in support of it. We then derive the model equations. A large part of the model development time was spent on parameter estimation. The majority of information in the bone biology literature is in the form of qualitative information. We therefore had to adapt global optimization methods so that the optimization procedure is based on qualitative objectives. The goal was to search for appropriate parameter

values such that the model output mimics trends in the data rather than minimizing some distance with the data points. A series of 57 objectives were used to calibrate the model. Finally, we show some model simulations to illustrate how well the model is able to reproduce what is observed in reality, including continuous versus intermittent PTH administration. In Sect. 3 we present pharmacokinetic models of PTH(1–34), denosumab (a RANKL antibody) and romosozumab (a sclerostin antibody). These pharmacokinetic models were built on top of, and thus dependent on, the biological model described in Sect. 2. For this reason, the pharmacokinetic models may only be successfully calibrated if the underlining biological model is an appropriate representation of the biological system, providing an additional element of validation (when considered together with the other elements of validation we provide). In Sect. 4, we use the model to simulate 5 major causes of osteoporosis, namely estrogen deficiency, senescence, glucocorticoid-induced osteoporosis, hyperparathyroidism and vitamin D deficiency. In Sect. 5, we explore dosing regimens for all these categories of osteoporosis based on the 3 drugs we included in the model: PTH(1–34), denosumab or romosozumab. Using the pharmacokinetic models, we investigate mono-therapies and combination therapies based on human doses and dosing regimen in function of disease severity. In Sect. 6, we propose an assessment of the model regarding aspects of validation.

2 Biological Model

2.1 Biology and Model Development

The model builds on the foundation of a previous model by integrating new knowledge of the biological system. The structure of the new model is presented in Fig. 1, which incorporates some important modifications compared to the initial version of the model (Lemaire et al. 2004). Here, we explain these changes for each pathway, starting with the RANK/RANKL/OPG pathway.

2.1.1 The RANK/RANKL/OPG Pathway

In our original paper, RANKL was solely produced by active osteoblasts and OPG was only secreted by responding osteoblasts (Lemaire et al. 2004). At the time, it was more of a modeling choice than one based on experimental evidence, since it was unclear if either of these cytokines was mostly produced by one cell type or by both. This original structure also appeared more robust dynamically. In earlier versions of the current model, we tried a different regulatory structure with both active osteoblasts and responding osteoblasts producing RANKL and OPG at a constant, but different rate, depending on the cell type. The idea was to let the optimization procedure search for the structure that would best represent what is observed biologically. Even after intensive optimization search, we did not find a case suggesting that having both active osteoblasts and responding osteoblasts producing both RANKL and OPG could lead to a better representation of the biological system. In all our optimization runs, the optimal structure was always the one with no RANKL produced by responding osteoblasts and

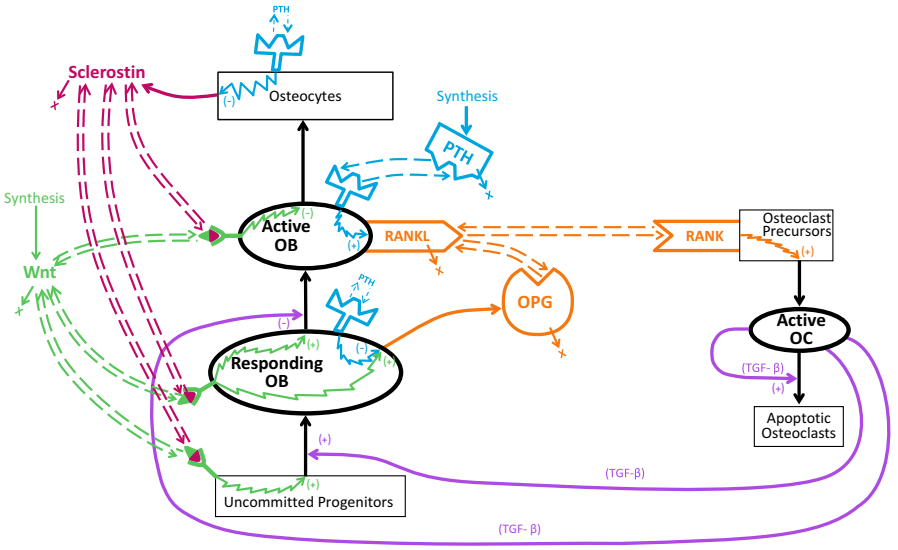

Fig. 1 Diagrammatic representation of the structure of the model. The ovals represent cell compartments. The solid arrows represent flows of the pointed element. The solid arrows with a (+) (or (−)) sign next to them indicate a stimulatory (or inhibitory) action. The zigzag arrows represent intracellular signaling leading to an increasing (or a diminishing) production of the indicated agent. The small arrows pointing at an 'X' indicate an elimination flow. The double dashed arrows represent receptor/ligand binding. The thin squared frames indicate types of cells that are not included in the model as variables. Different colors are used for different pathways represented in the model. The RANK/RANKL/OPG pathway is represented in orange, the TGF-β pathway in purple, the PTH pathway in blue, the Wnt pathway in green, and the SOST pathway in red (Color figure online)

no OPG secreted by active osteoblasts. We therefore chose to maintain the original structure of the RANK/RANL/OPG pathway in the final version of the current model. Other authors have proposed a different structure to represent how RANKL and OPG are produced by cells of the osteoblast lineage (Pivonka et al. 2008, 2010).

2.1.2 The Wnt Pathway

Wnt proteins are secreted glycoproteins and are the mammalian homologs of the Drosophila morphogen Wingless (Gogakos et al. 2009). There are many variants of Wnt proteins, and they are involved in many pathways. The pathway of interest for bone homeostasis is the Wnt/β-Catenin pathway. Wnt binds to a co-receptor complex involving the Lpr5/Lpr6 receptor and one of the Frizzled family members, activating the β-Catenin pathway (Bonewald and Johnson 2008). Wnt binding enhances both the proliferation of pre-osteoblasts and the differentiation of osteoblasts into more mature cells, and inhibits osteoblast apoptosis (Daoussis and Andonopoulos 2011; Khosla et al. 2008). Wnt also promotes the expression of OPG in osteoblasts (Goldring and Goldring 2007). Wnt has also been reported to inhibit osteoclastogenesis but we believe, as do other authors, that this is an indirect effect of OPG outcompeting RANK for RANKL binding (Khosla et al. 2008; Kramer et al. 2010).

2.1.3 The SOST Pathway

Sclerostin is the product of the SOST gene. It is expressed almost exclusively in bone, specifically by osteocytes (Paszty et al. 2010). Sclerostin inhibits Wnt signaling in osteoblasts by binding the Lpr5/6 receptors, leading to decrease bone formation by osteoblasts (Ellies et al. 2006; Li et al. 2005).

2.1.4 The PTH Pathway

The representation of the action of PTH on osteoblast cells is unchanged from our original paper (Lemaire et al. 2004). PTH binding to its receptor on osteoblastic cells increases expression of RANKL but reduces expression of OPG (Gogakos et al. 2009; Kramer et al. 2010). A new addition is the binding of PTH expressed by osteocytes (Fermor and Skerry 1995). In this cell type, PTH signaling downregulates the SOST gene (Keller and Kneissel 2005), reducing production of sclerostin (Bellido et al. 2005).

2.1.5 Continuous Versus Intermittent PTH

Continuous administration of PTH results in increased osteoclastogenesis and bone resorption (Gogakos et al. 2009). By contrast, intermittent PTH (e.g., one injection per day) leads to increased bone formation (Gogakos et al. 2009). In fact, both osteoblast and osteoclast activities are increased during intermittent PTH, but the overall effect on bone mass is anabolic (Kramer et al. 2010). The molecular and cellular mechanisms underlying the differential effects of PTH administration have not been clearly established, despite some putative explanations proposed in the literature (Bellido et al. 2003; Jilka 2007; Potter et al. 2005). The addition of the Wnt pathway, the SOST pathway, and the PTH pathway acting on the osteocytes provides wider range of action for PTH. PTH leads to osteoclastogenesis through the RANK/RANKL/OPG pathway, but also leads to osteoblastogenesis though the Wnt/SOST pathway. We think the activation of osteoclasts though the RANK/RANKL/OPG pathway should be slower than the activation of osteoblasts through the Wnt/SOST pathway, because RANK/RANKL/OPG pathway activation is mainly operated via cell–cell contact in the bone remodeling canopy (Furuya et al. 2018). In this paper, we show that the difference in activation kinetics between the RANK/RANKL/OPG pathway and the Wnt/SOST pathway could be the basis of the differential action of PTH. The idea that the interplay between slow and fast activation kinetics could lead to differential effects of PTH has been considered previously, but based on different mechanisms. In (Cho et al. 2000), it was postulated that there are two types of PTH receptors, one with slow binding kinetics and another with fast binding kinetics. A difference in PTH administration (continuous vs. intermittent) would produce different binding patterns in the population of receptors, generating different intracellular signaling and different cell responses (Potter et al. 2005). More recently, Ross et al. incorporated mechanisms for the differential action of PTH in a model of bone cells dynamics (Ross et al. 2012). Their approach is based on findings by Bellido et al. (2003) who argued that PTH reduces the rate of apoptosis of osteoblasts. In Bellido et al. (2003), exposure to PTH

would lead to a fast decrease in Runx2 protein (which reduces osteoblast apoptosis) followed by a slow recovery of Runx2 level to baseline, even when PTH administration is sustained. This fast/slow kinetics in response to PTH exposure can produce the kind of differential effect observed in continuous versus intermittent administration of PTH, as shown by the modeling of Ross et al. (2012). The Runx2 mechanism proposed by Bellido et al. (2003) was previously incorporated in an integrated calcium homeostasis and bone remodeling model (Peterson and Riggs 2010). Our findings, based on a mathematical model, indicate that the differential action of PTH may not be the result of an additional extraneous pathway, but would be intrinsic to the core regulation of the bone cells, occurring through the difference in activation kinetics between the RANK/RANKL/OPG pathway and the Wnt/SOST pathway.

2.2 Model Equations

The mathematical formalism used for the model is similar to the one of our earlier paper (Lemaire et al. 2004). The dynamics of bone cell densities is represented by ordinary differential equations that account for the time evolution of the bone cells in the model. Three cell types are represented in the model as state variables. The active osteoblasts (B) are actively forming bone. The so-called responding osteoblasts (R) are less mature osteoblasts (or pre-osteoblasts) that respond differentially to pro or anti-osteoblastic signals and differentiate into active osteoblasts. The active osteoclasts (C) are actively resorbing bone. The set of differential equations are shown in (1).

$$\begin{cases} \frac{\mathrm{d}R}{\mathrm{d}T} = D_R \cdot \pi_C \cdot \pi_W - D_B \cdot \frac{\pi_W}{\pi_C} \cdot R \\ \frac{\mathrm{d}B}{\mathrm{d}T} = D_B \cdot \frac{\pi_W}{\pi_C} \cdot R - \frac{k_e^B \cdot B}{\pi_W} \\ \frac{\mathrm{d}C}{\mathrm{d}T} = D_C \cdot \pi_L - k_e^C \cdot \pi_C \cdot C \end{cases} \tag{1}$$

D_R, D_B, and D_C are constant differentiation rates, k_e^B and k_e^C are constant elimination rates.

We assume that cell response triggered by cytokine binding to their membrane receptors depends on receptor occupancy (Lemaire et al. 2004). Receptor occupancy is represented by the π functions in Eq. (1). These functions represent the ratio between occupied receptors and the total number of receptors, so they go from 0, when no receptor is occupied, to 1, when all receptors are occupied. π_C represents the TGF-β receptor occupancy, although TGF-β is not strictly represented in the model. π_W is the Wnt receptor occupancy by Wnt proteins and π_L is the RANK occupancy by RANKL. As argued in (Lemaire et al. 2004), "proliferative" cell response is proportional to receptor occupancy, whereas "anti-proliferative" cell response is inversely proportional to receptor occupancy. Based on these few statements, the equations in (1) can be directly derived from the model structure in Fig. 1.

TGF-β is embedded within the bone matrix and is released in the bone microenvironment when bone is degraded by osteoclasts. We assume that the rate of release

of TGF-β per osteoclast is constant, and that the binding of TGF-β to its receptor is faster than changes in cell numbers. Therefore, the concentration of TGF-β released from the bone matrix by osteoclasts should be well correlated with the local density in active osteoclasts. We thus assume that the TGF-β concentration is proportional to the density in active osteoclasts. The TGF-β receptor occupancy is then given by the following relation (Lemaire et al. 2004):

$$\pi_C = \frac{C + f_0 \cdot C_{50}}{C + C_{50}}, \tag{2}$$

where C_{50} is the equivalent of the dissociation coefficient of TGF-β with its receptor (it is in reality the osteoclast density to achieve half TGF-β receptor occupancy). f_0 is the minimal TGF-β receptor occupancy (f_0 is assumed much smaller than 1).

The binding scheme of Wnt, sclerostin and a possible anti-sclerostin antibody is represented in Fig. 2. The binding of Wnt to the LPR5/6 receptor may be written as

$$W + W_r \underset{k_8}{\overset{k_7}{\rightleftarrows}} W_r \circ W, \tag{3}$$

where W is the basal concentration of Wnt (which is constant, reflecting the undiminished availability of Wnt, see Fig. 2), W_r is the LPR5/6 receptor and $W_r \circ W$ their complex. At steady state, we have

$$W \cdot W_r = k_D^W \cdot W_r \circ W, \tag{4}$$

where $k_D^W = {}^{k_8}/_{k_7}$. The binding schemes for sclerostin with LPR5/6 and for sclerostin with its antibody are

$$S + W_r \underset{k_{10}}{\overset{k_9}{\rightleftarrows}} W_r \circ S, \tag{5}$$

$$S + \alpha S \underset{k_{14}}{\overset{k_{13}}{\rightleftarrows}} \alpha S \circ S. \tag{6}$$

The differential equations for $W_r \circ S$ and $\alpha S \circ S$ are

$$\frac{\mathrm{d}W_r \circ S}{\mathrm{d}t} = k_9 \cdot S \cdot W_r - k_{10} \cdot W_r \circ S, \tag{7}$$

$$\frac{\mathrm{d}\alpha S \circ S}{\mathrm{d}t} = k_{13} \cdot S \cdot \alpha S - k_{14} \cdot \alpha S \circ S - k_e^{\alpha S \circ S} \cdot \alpha S \circ S, \tag{8}$$

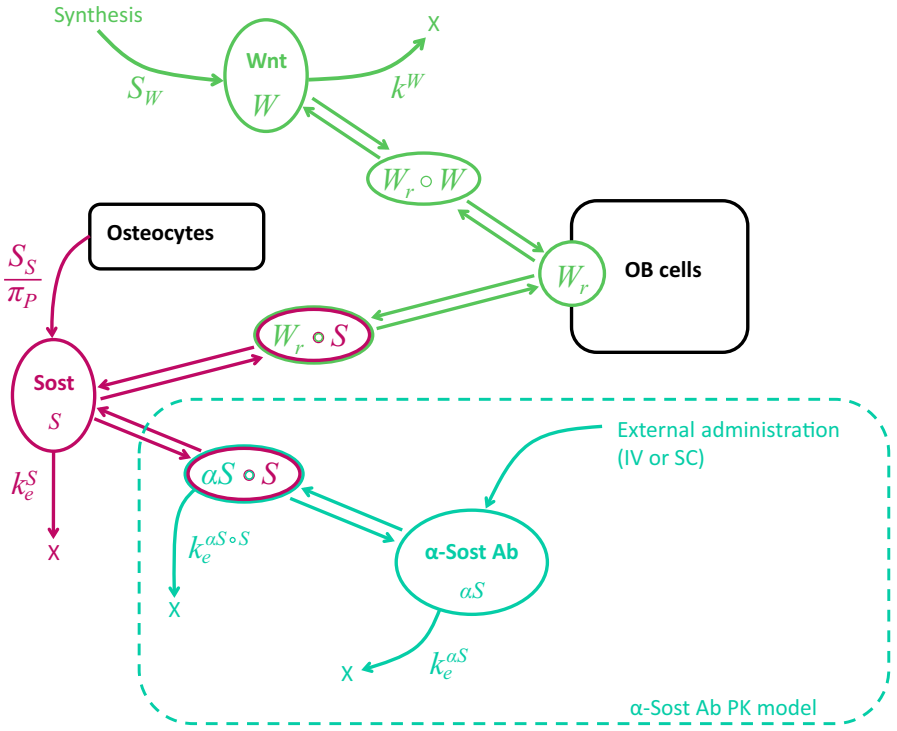

Fig. 2 Representation of the Wnt/SOST binding scheme in the model. The scheme includes a possible administration of an anti-sclerostin antibody neutralizing sclerostin (the SOST product). $\boldsymbol{S_W}$ (resp. $\boldsymbol{k^W}$) represents the rate of synthesis (resp. degradation) of the Wnt molecules. These 2 parameters and are shown here for illustration only since the Wnt level is assumed constant throughout our analysis

where αS is a sclerostin antibody and $k_e^{\alpha S \circ S}$ is the degradation rate of the antibody bound to its target. The differential equation for the sclerostin concentration is

$$\frac{\mathrm{d}S}{\mathrm{d}t} = I_S + \frac{S_S}{\pi_P} - k_e^S \cdot S + k_{14} \cdot \alpha S \circ S - k_{13} \cdot S \cdot \alpha S + k_{10} \cdot W_r \circ S - k_9 \cdot S \cdot W_r, \tag{9}$$

where S_S/π_P is the rate of synthesis of sclerostin by osteocytes in response to PTH binding, S_S is the unperturbed rate of synthesis of sclerostin, I_S is an optional external rate of administration of sclerostin, and k_e^S is the rate of elimination of sclerostin. Taking (7), (8) and (9) at steady state we have

$$k_{10} \cdot W_r \circ S = k_9 \cdot S \cdot W_r, \tag{10}$$

$$k_{14} \cdot \alpha S \circ S - k_{13} \cdot S \cdot \alpha S = -k_e^{\alpha S \circ S} \cdot \alpha S \circ S, \tag{11}$$

$$I_S + \frac{S_S}{\pi_P} - k_e^S \cdot S = k_e^{\alpha S \circ S} \cdot \alpha S \circ S. \tag{12}$$

Substituting (11) in (12), we obtain

$$\left(I_S + \frac{S_S}{\pi_P} - k_e^S \cdot S\right) \cdot \left(k_{14} + k_e^{\alpha S \circ S}\right) = k_e^{\alpha S \circ S} \cdot k_{13} \cdot S \cdot \alpha S, \tag{13}$$

which can be rewritten as

$$S = \left(\frac{S_S/k_e^S}{\pi_P} + \frac{I_S}{k_e^S}\right) \cdot \frac{1}{\frac{\alpha S}{\kappa_1} + 1}, \tag{14}$$

where

$$\kappa_1 = \frac{k_e^S \cdot \left(k_{14} + k_e^{\alpha S \circ S}\right)}{k_{13} \cdot k_e^{\alpha S \circ S}}. \tag{15}$$

The total number of Wnt receptors (LPR5/6 receptors) is

$$W_r^T = W_r + W_r \circ W + W_r \circ S. \tag{16}$$

Substituting (4) and (10) into (16), we obtain

$$W_r^T = \frac{k_D^W}{W} \cdot W_r \circ W + W_r \circ W + \frac{S}{k_D^S} \cdot \frac{k_D^W}{W} \cdot W_r \circ W, \tag{17}$$

where $k_D^S = k_{10}/k_9$.

By definition, the Wnt receptor occupancy by Wnt is $\pi_W = \frac{W_r \circ W}{W_r^T}$. Dividing (17) by W_r^T we obtain

$$1 = \pi_W \cdot \left(\frac{k_D^W}{W} + 1 + \frac{S}{k_D^S} \cdot \frac{k_D^W}{W}\right). \tag{18}$$

Injecting (14) into (18), we finally obtain

$$\pi_W = \frac{K_D^W}{K_D^W + K_D^S \cdot \left(\frac{1}{\pi_P} + i_S\right) \cdot \frac{1}{\frac{\alpha S}{\kappa_1} + 1} + 1}, \tag{19}$$

where $K_D^W = \frac{W}{k_D^W}$, $K_D^S = \frac{S_S/k_e^S}{k_D^S}$ and $i_S = \frac{I_S}{S_S}$. We see that the fraction of occupied Wnt receptors by Wnt depends on 3 constant parameters (K_D^W, K_D^S and κ_1), the PTH receptors occupancy π_P, an optional external rate of administration of sclerostin i_S, and the concentration of the sclerostin antibody αS, which is given by a pharmacokinetic model (see Sect. 3.3).

The binding scheme of PTH with its receptor is (Lemaire et al. 2004)

$$P + P_r \underset{k_6}{\overset{k_5}{\rightleftarrows}} P_r \circ P. \tag{20}$$

The differential equation for the complex $P_r \circ P$ is

$$\frac{\mathrm{d}P_r \circ P}{\mathrm{d}t} = k_5 \cdot P \cdot P_r - k_6 \cdot P_r \circ P, \tag{21}$$

and the total number of PTH receptor is $P_r^T = P_r + P_r \circ P$. We assume that (21) equilibrates faster than changes in P. Considering (21) at steady state gives

$$P_r^T = P_r \circ P \cdot \left(\frac{k_D^P}{P} + 1 \right), \tag{22}$$

where $k_D^P = {k_6}/{k_5}$. The PTH receptor occupancy is $\pi_P = \frac{P_r \circ P}{P_r^T}$, so from (22) we have

$$\pi_P = \frac{P}{P + k_D^P}. \tag{23}$$

We can decompose the PTH concentration into two components as the sum of the endogenous PTH P_b and PTH coming from an external source P_i (e.g., a subcutaneous injection of PTH(1–34)). Since PTH(1–34) and PTH(1–84) have the same binding sequence with respect to the PTH receptor, they are treated the same way in the model. In that case, substituting P by $P_b + P_i$ in (23), and dividing by P_b, we obtain

$$\pi_P = \frac{1 + \frac{P_i}{P_b}}{1 + \frac{P_i}{P_b} + K_D^P}, \tag{24}$$

where $K_D^P = {k_D^P}/{P_b}$. We see that π_P depends on 2 constant parameters (P_b and K_D^P) and P_i, which is given by a pharmacokinetic model (see Sect. 3.1).

The only binding kinetics we do not consider at steady state is the binding of RANK and RANKL. Their binding requires cell-to-cell contact between osteoblasts and osteoclasts so it should be slower than binding involving soluble ligands or receptors. The binding scheme of RANKL with RANK is

$$K + L \underset{k_4}{\overset{k_3}{\rightleftarrows}} K \circ L. \tag{25}$$

We assume that law of mass action applies for reaction scheme (25) so the differential equation for the $K \circ L$ complex is

$$\frac{\mathrm{d}K \circ L}{\mathrm{d}t} = k_3 \cdot K \cdot L - k_4 \cdot K \circ L. \tag{26}$$

The RANK concentration K is not a state variable and is assumed constant to reflect the undiminished availability of the osteoclast precursors. And L is the RANKL concentration calculated at steady state in Eq. (36) below. The RANK occupancy is labeled π_L and is given by

$$\pi_L = \frac{K \circ L}{K + K \circ L}. \tag{27}$$

$K \circ L$ is calculated by solving (26).

RANKL is a membrane-bound ligand attached on the surface of osteoblasts. We assume that each osteoblast cell can support a maximum number of RANKL attached to their surface (maximum carrying capacity) which we call $K^L_{\max}$. As it was said in Sect. 2.1, the actual number of RANKL attached to the surface of each osteoblast depends on PTH receptor occupancy. The rate of change of RANKL is then represented by the following expression (Lemaire et al. 2004)

$$r_L \times \left(1 - \frac{L + O \circ L + K \circ L + \alpha L \circ L}{K^L_{\max} \cdot \pi_P \cdot B}\right) + I_L, \tag{28}$$

where r_L is the rate of production of RANKL and I_L is an optional external rate of administration of soluble RANKL. Since the membrane-bound RANKL is either free or bound, $L + O \circ L + K \circ L + \alpha L \circ L$ represents the total number of membrane-bound RANKL, where $\alpha L \circ L$ is the complex formed by RANKL and an anti-RANKL antibody (externally administrated in the system) and $O \circ L$ is the complex formed by OPG and RANKL. At steady state, RANKL level does not change so the net rate in expression (28) is zero, thus we have

$$L + O \circ L + \alpha L \circ L = (i_L + 1) \cdot K^L_{\max} \cdot \pi_P \cdot B - K \circ L, \tag{29}$$

where $i_L = {I_L}/{r_L}$. The binding schemes for OPG with RANKL and RANKL with its antibody are

$$O + L \underset{k_2}{\overset{k_1}{\rightleftarrows}} O \circ L, \tag{30}$$

$$L + \alpha L \underset{k_{12}}{\overset{k_{11}}{\rightleftarrows}} \alpha L \circ L. \tag{31}$$

Taking (30) and (31) at steady state gives

$$O \circ L = \frac{O}{k^O_D} \cdot L, \tag{32}$$

where $k_D^O = {}^{k_2}/_{k_1}$, and

$$\alpha L \circ L = \frac{\alpha L}{k_D^{\alpha L}} \cdot L, \tag{33}$$

where $k_D^{\alpha L} = {}^{k_{12}}/_{k_{11}}$. OPG is secreted by responding osteoblasts and its secretion is represented as a function of the Wnt receptor occupancy and the PTH receptor occupancy (see Sect. 2.1). The net rate of change of OPG is thus given by

$$r_O \cdot \frac{\pi_W}{\pi_P} \cdot R + I_O - k_e^O \cdot O, \tag{34}$$

where r_O is the rate of production of OPG, k_e^O is the rate of elimination of OPG, and I_O is an optional external rate of administration of OPG. At steady state, the rate in (34) is zero, and this gives

$$O = \frac{\frac{\pi_W}{\pi_P} \cdot R + \frac{I_O}{r_O}}{{}^{k_e^O}/_{r_O}} \tag{35}$$

Substituting (32), (35) and (33) into (29) gives the relation for L,

$$L = \frac{(i_L + 1) \cdot K_{max}^L \cdot \pi_P \cdot B - K \circ L}{1 + \frac{\frac{\pi_W}{\pi_P} \cdot R}{K_D^O} + i_O + \frac{\alpha L}{k_D^{\alpha L}}} \tag{36}$$

where $K_D^O = \frac{k_D^O \cdot k_e^O}{r_O}$ and $i_O = \frac{I_O}{K_D^O \cdot r_O}$.

In summary, the model equations correspond to the differential Eqs. (1) and (26), the receptor occupancy functions (2), (19), (24) and (27), and an additional relation for the RANKL concentration (36). i_L, i_O and i_S are optional external inputs of RANKL, OPG, and sclerostin, respectively, summarized in Table 1. In these equations, P_i, αL and αS are given by the pharmacokinetic models presented in Sect. 3. All model parameters are summarized in Tables 2, 3 and 4 with their value of reference.

Table 1 These parameters are optional inputs for RANKL, OPG and sclerostin respectively

Symbol	Unit	Typical value	Description
i_L	None	4	Administration of RANKL into the bone compartment [see Eq. (36)]
i_O	None	20	Administration of OPG into the bone compartment [see Eq. (36)]
i_S	None	80	Administration of sclerostin into the bone compartment [see Eq. (19)]

They were added to the model to allow perturbation of inherent levels of RANKL, OPG or sclerostin in one way or another. These inputs may be held constant or may depend on time to simulate temporary stimulus or time-dependent inputs. Typical values are indicated for each input

Table 2 These are the parameters of the bone model which were determined by optimization (fitting parameters)

Symbol	Unit	Value	Description
D_R	pM/day	1.28×10^{-4}	Differentiation rate of osteoblast progenitors into responding osteoblasts [see Eq. (1)]
f_0	None	3.39×10^{-2}	Minimal TGF-β receptor occupancy [see Eq. (2)]
C_{50}	pM	1.25×10^{-6}	Osteoclast density to achieve half TGF-β receptor occupancy [see Eq. (2)]
D_B	day^{-1}	3.47	Differentiation rate of responding osteoblasts into active osteoblasts [see Eq. (1)]
k_e^B	day^{-1}	1.21×10^{-3}	Rate of elimination/death of active osteoblasts [see Eq. (1)]
D_C	pM/day	7.12×10^{-3}	Differentiation rate of osteoclast progenitors into active osteoclasts [see Eq. (1)]
k_e^C	day^{-1}	6.46×10^{-2}	Rate of elimination/death of active osteoclasts [see Eq. (1)]
K_D^O	pM	4.76×10^{-6}	Mixed parameter representing a typical density of OPG-producing cells [see Eq. (36)]
K_{max}^L	pmol/pmol of cells	4644.6	Maximum carrying capacity of cell-bound RANKL by osteoblasts [see Eq. (28)]
k_3	$\text{pM}^{-1}\ \text{day}^{-1}$	0.368	RANK-RANKL association rate [Eq. (25)]
k_4	day^{-1}	65.64	RANK-RANKL dissociation rate [Eq. (25)]
K_D^P	None	20.17	Mixed parameter related to unbound PTH receptors in basal condition [see Eq. (24)]
K	pM	0.10	RANK density [see Eq. (26)]
K_D^S	None	14.95	Mixed parameter related to unbound sclerostin molecules in basal condition [see Eq. (19)]
K_D^W	None	3.70	Mixed parameter related to unbound Wnt molecules in basal condition [see Eq. (19)]

The bone model is presented in Sect. 2.2. The optimization procedure is presented in Sect. 2.3. The numerical values resulting from the optimization procedure are indicated below for each parameter. These values may be considered the values of reference; they correspond to typical values for a healthy subject. Some of these values are discussed in Sect. 6 as part of the model assessment and validation

2.3 Parameter Estimation

The model presented in Sect. 2.2 contains 16 parameters. This does not count the parameters of the PK models (Sect. 3), which adds another 20 parameters. Most of these parameters do not have a known value or cannot be estimated easily from the literature. Experimental determination of model parameters can be quite difficult since it might not be possible to isolate the process represented by a parameter in an experiment. In our earlier paper, acceptable ranges for the model parameters were deduced from information in the literature and final numerical values were determined by "manual" optimization (Lemaire et al. 2004). However, optimizing a dynamical system for its parameters "by hand" is a tedious, laborious and time-consuming task.

Table 3 These are the parameters of the PK models which were determined by optimization (fitting parameters)

Symbol	Unit	Value	Description
V_d^P	L	9.08	Volume of distribution of PTH (see Fig. 6)
k_{12}^P	day^{-1}	89.32	Rate of transfer of PTH from the blood circulation to tissues (see Fig. 6)
k_{21}^P	day^{-1}	31.47	Rate of transfer of PTH from tissues to the blood circulation (see Fig. 6)
k_e^P	day^{-1}	151.64	Rate of elimination of PTH from the blood circulation (see Fig. 6)
k_a^P	day^{-1}	27.85	Rate of absorption of PTH from the subcutaneous site of injection to the blood circulation (see Fig. 6)
$V_d^{\alpha L}$	L	4.12	Volume of distribution of denosumab (see Fig. 10-a)
$k_e^{\alpha L}$	day^{-1}	0.019	Rate of elimination of denosumab from the blood circulation (see Fig. 10-a)
$k_e^{\alpha L \circ L}$	day^{-1}	6.65×10^4	Rate of elimination of denosumab bound to target RANKL from the blood circulation (see Fig. 10-a)
$k_a^{\alpha L}$	day^{-1}	0.77	Rate of absorption of denosumab from the subcutaneous site of injection to the blood circulation (see Fig. 10-a)
$k_D^{\alpha L}$	pM	6.57×10^2	Dissociation coefficient of denosumab with its target RANKL [see Eq. (33)]
$V_d^{\alpha S}$	L	6.22	Volume of distribution of romosozumab (see Fig. 10-b)
$k_e^{\alpha S}$	day^{-1}	0.025	Rate of elimination of romosozumab from the blood circulation (see Fig. 10-b)
$k_a^{\alpha S}$	day^{-1}	0.57	Rate of absorption of romosozumab from the subcutaneous site of injection to the blood circulation (see Fig. 10-b)
$F^{\alpha S}$	none	0.69	Bioavailability of romosozumab after subcutaneous injection (see Fig. 10-b)
κ_1	pM	6.48×10^4	Mixed parameter representing a typical romosozumab concentration [see Eq. (15)]
κ_2^0	day^{-1}	6.58×10^{-3}	Maximum κ_2 value [see Eq. (42)]. κ_2 is a mixed parameter representing a typical dissociation rate related to romosozumab [see Eq. (41)]
κ_2^{50}	pmol	1.49×10^5	romosozumab dose leading to half saturation of κ_2 value [see Eq. (42)]
κ_2^{min}	day^{-1}	4.3×10^{-3}	Minimum κ_2 value [see Eq. (42)]

The PK models are presented in Sects. 3.1, 3.2 and 3.3 for PTH, denosumab, and romosozumab, respectively. The optimization procedure is presented in Sect. 2.3. The numerical values resulting from optimization procedure are indicated below for each parameter. These values may be considered the values of reference; they correspond to typical values for a healthy subject. Some of these values are discussed in Sect. 6 as part of the model assessment and validation

Table 4 The values of these parameters were estimated from the literature (non-fitting parameters)

Symbol	Unit	Value	Description
P_b	pM	3.2	Basal endogenous PTH concentration [see Eq. (24)] (Aloia et al. 2006)
F^P	None	0.95	Bioavailability of PTH after subcutaneous injection (see Fig. 6) (Clausen 2009)
$F^{\alpha L}$	None	0.64	Bioavailability of denosumab after subcutaneous injection (see Fig. 10a) (Sutjandra et al. 2011)

Key references for these values are indicated for each parameter

It requires large quantities of visualization and monitoring operations to bring the system at a proper location of the parameter space.

Most information available in the literature on bone biology is in the form of qualitative information. In typical biological experiments, perturbations are applied to a system and the response of the system is measured as a change in the trend of a measured variable. For example, the expression of a protein of interest could be increasing or decreasing from baseline. Information is less often given as absolute values, such as the concentration of a compound in pharmacokinetic studies or the absolute level of a biomarker. In numerical optimization, the distance between the expected value of a model variable and the expression of that variable in an experiment is minimized by adjusting the values of the model parameters. If the data is not given as an absolute quantity at a given time point, but rather as a trend evolution from baseline, numerical optimization is not directly applicable. That was the main reason why we had to rely on "manual" optimization for parameter estimation for our earlier model (Lemaire et al. 2004).

2.3.1 Optimization Based on Qualitative Objectives

In the present model, the number of unknown parameters to estimate is larger and there are more data to incorporate in the model. Manual optimization is no longer feasible. In order to estimate our model parameters, we developed a series of multi-objective optimization algorithms based on qualitative objectives. We will not present these optimization methods in detail since it would be out of the scope of the present article. The main difficulties we faced were dealing with ambiguity in data trends and the non-uniqueness of ways to follow a single trend. Most of these difficulties were ironed out by two factors. First, our bone model is almost purely mechanistic and, as such, the possible behaviors that the model may generate for different parameter values is constrained and limited by these mechanisms. Second, the number of qualitative objectives used for the optimization is large and diverse, which further constrains the valid possibilities in the parameter space.

Based on what is known in the literature about the bone remodeling system, we identified a series of 11 experiments with known outcomes, which are our qualitative objectives. The model was then optimized to behave similarly to what is observed in the real system after perturbations are applied (i.e., the experiments). Each experiment

is defined by the type of perturbations that are applied; and for each experiment, we define a set of objectives representing what is observed in the real world. The hard part is to identify the proper set of experiments/objectives that should be performed, and adjust each objective such that it is not too strict or too loose to allow the system to follow a successful optimization path.

Although quite different in nature, another approach, to make optimization of the model parameters tractable, is to use a population approach. In this approach, a reduced version of the model is considered, with a much smaller number of parameters. The mechanistic cohesion of the original model is lost, but the essential dynamics is preserved (Schmidt et al. 2011). Because of the limited number of parameters in the reduced model, it is possible to optimize the model on a large number of individual patient data (Berkhout et al. 2015). This approach allows inferring statistical correlations between model outputs and population covariates, and developing statistical claims between dose and some model outputs. A (virtual) population approach can also be performed using a fully mechanistic model (with potentially a large number of parameters). In that case, the population variability is not estimated from individual patient data, but is reconstructed to match clinical endpoints statistics from a real patient population (Allen et al. 2016; Gadkar et al. 2014).

We refer to supplementary information for a discussion on using bone formation and bone resorption biomarker data for model calibration or for verifying the current calibration.

2.3.2 Optimization of the Bone Model

We summarized all 11 experiments and a total of 57 objectives in Table 5. The first experiment corresponds to the unperturbed state in which we just observe bone cell densities and check that they are within acceptable physiological ranges. There is some information in the literature about values of bone cell densities under "normal" conditions. For example, in the paper by Wang et al. (Table 2 inside reference (Wang et al. 2011)), cell densities of active osteoblasts, active osteoclasts and responding osteoclasts are estimated at about 10^{-4} pM. We did not want to calibrate the model at specific values of bone cell densities to avoid over constraining the model and because bone cell densities are highly variable under different physiological or experimental conditions. Instead, we used a range of acceptable values as shown in Table 5. Another objective for the unperturbed state is that the time to reach steady state T_{SS} is less than 500 days (in that case, T_{SS} refers to the time to reach steady state from initial conditions which were chosen at the border of the range of acceptable cell densities). In the remaining 10 experiments of Table 5, it is also required that the time to reach steady state is less than 500 days. In those cases, T_{SS} refers to the time to reach steady state of the perturbed state, starting from the steady state of the unperturbed state. Typical time frame for bone remodeling in the BMU (Basic Multicellular Unit) is on the order of 100 days (Vacanti and Pietrzak 2008). So 500 days is a rather conservative upper limit for the duration of bone remodeling processes at the cellular scale; but it is still helpful in constraining the search space. Objectives of the form $R \nearrow$, $B \nearrow$, $C \nearrow$ or $C/B \searrow$ in Table 5 indicate that significant increase (or decrease, depending on the arrow) in the steady-state value of the men-

tioned species should be observed after perturbations are applied. These behaviors reflect the tight coupling in the activities of the bone cells, as supported by the literature presented in our earlier paper (Sect. 3 inside reference Lemaire et al. 2004). The objective $\max(\pi_C)/\min(\pi_C) > 1.5$ after increasing or decreasing the population of active osteoclast is to ensure that significant changes in active osteoclast density is well reflected at the level of π_C, which represents TGF-β receptor occupancy. Objectives of the kind $\pi_{P,L,W}|_{\text{per,ref}}/\pi_{P,L,W}|_{\text{ref,per}} >$ number have the same purpose, which is to make sure that the outcomes of perturbations are reflected at the level of receptor occupancy. The objective $\pi_W/\pi_P|_{\text{ref}}/\pi_W/\pi_P|_{\text{per}} > 1.5$ after administration of continuous PTH is there to favor sets of parameters promoting RANKL concentration, as opposed to smaller RANKL levels under basal PTH conditions. Looking at Eq. (36), you see that a smaller ratio π_W/π_P will lead to higher RANKL level, which in turn will favor osteoclastogenesis. Finally, the objective $\pi_W/\pi_P|_{\text{per}}/\pi_W/\pi_P|_{CP} > 1.5$ after intermittent administration of PTH should favor sets of model parameters during optimization leading to smaller RANKL concentration, which should lead to more limited osteoclastogenesis (see the paragraph about intermittent PTH in Sect. 2.1 for more explanations).

2.3.3 Optimization of the PK Models

For the optimization of the PK models, the fitness function used was the distance between the PK data in Figs. 5, 8 and 9 and corresponding model curves (typical least squares minimization approach). The optimization method used was a modified Nelder-Mead simplex method combined with Monte Carlo sweeping of random subdomains of the parameter space. For the optimization of the bone model, we used a multi-objective genetic algorithm with custom creation and crossover functions. We modified the method to take into account fitness functions based on the type of qualitative objectives presented just above. We also used random generation of initial populations with auto-adaptive a priori knowledge of parameter distributions.

All the parameters of the bone model presented in Sect. 2.2 were determined by global optimization using the optimization methods mentioned above and the qualitative objectives presented in Table 5. There are a total of 15 fitting parameters in the bone model; they are recapitulated in Table 2 with their value of reference determined from the optimization procedure. One parameter of the bone model, the average endogenous PTH serum level (Table 4), was obtained directly from the literature (Aloia et al. 2006). With this set of parameter values, the model successfully satisfied all 57 objectives in Table 5. We also verified that these parameter values are well within physiological range known in the literature (see the model assessment in Sect. 6).

Although the PK models are not independent of the bone model, as explained in Sects. 3.2 and 3.3, we determined the parameters of the PK models separately from the parameter fitting procedure of the bone model. This was possible because the bone model does not need any anti-RANKL antibody or anti-sclerostin antibody to function. However, the injection of an anti-RANKL antibody or anti-sclerostin antibody needs both the PK models and the bone model to generate an output. Thus, while the parameter fitting of the PK models is based on the PK data shown in Figs. 5, 8 and 9, it uses both the PK models and the previously optimized bone model in the

Table 5 The list of qualitative objectives used for the optimization of the model is summarized in this table

Experiment	Perturbations	Objectives
① Monitoring cell densities	None (unperturbed state)	10^{-5} pM $\leq \max(R, B, C) \leq 10^{-2}$ pM and 10^{-6} pM $\leq \min(R, B, C) \leq 10^{-3}$ pM $T_{ss} < 500$ days
② Addition of active osteoblasts	Adding active osteoblasts at the rate ${}^{B\vert \text{ref}}/_{8}$ per day	$R \nearrow$ $B \nearrow$ $C \nearrow$ ${}^{C}/_{B} \searrow$ $T_{ss} < 500$ days
③ Addition of active osteoclasts	Adding active osteoblasts at the rate ${}^{C\vert \text{ref}}/_{8}$ per day	$R \nearrow$ $B \nearrow$ $C \nearrow$ ${}^{C}/_{B} \nearrow$ $T_{ss} < 500$ days $\frac{\max(\pi_C)}{\min(\pi_C)} > 1.5$
④ Addition of responding osteoblasts	Adding active osteoblasts at the rate ${}^{R\vert \text{ref}}/_{8}$ per day	$R \nearrow$ $B \nearrow$ $T_{ss} < 500$ days
⑤ Lowering active osteoblasts	$k_e^B\vert_{\text{per}} = 4 \cdot k_e^B\vert_{\text{ref}}$	$R \searrow$ $B \searrow$ $C \searrow$ ${}^{C}/_{B} \nearrow$ $T_{ss} < 500$ days
⑥ Lowering active osteoclasts	$k_e^C\vert_{\text{per}} = 8 \cdot k_e^C\vert_{\text{ref}}$ and $D_C\vert_{\text{per}} = {}^{D_C\vert \text{ref}}/_{8}$	$R \searrow$ $B \searrow$ $C \searrow$ ${}^{C}/_{B} \searrow$ $T_{ss} < 500$ days $\frac{\max(\pi_C)}{\min(\pi_C)} > 1.5$
⑦ Lowering responding osteoblasts	$D_R\vert_{\text{per}} = {}^{D_R\vert \text{ref}}/_{4}$	$R \searrow$ $B \searrow$ $T_{ss} < 500$ days
⑧ Continuous administration of PTH	PTH is added continuously at 4 times the rate of endogenous PTH synthesis (which leads to PTH levels symptomatic of hyperparathyroidism)	$R \nearrow$ $B \nearrow$ $C \nearrow$

Table 5 continued

Experiment	Perturbations	Objectives
		$C/B \nearrow$ $T_{ss} < 500$ days $\frac{\pi_P\|_{\text{per}}}{\pi_P\|_{\text{ref}}} > 3$ $\frac{\pi_L\|_{\text{per}}}{\pi_L\|_{\text{ref}}} > 3$ $\frac{\frac{\pi_W}{\pi_P}\|_{\text{ref}}}{\frac{\pi_W}{\pi_P}\|_{\text{per}}} > 1.5$
⑨ Intermittent administration of PTH	PTH is injected subcutaneously at 20 μg once a day (which is the recommended dosing for teriparatide) 'CP' refers to a value at steady state during continuous administration of PTH	$R \nearrow$ $B \nearrow$ $C \nearrow$ $C/B \searrow$ $T_{ss} < 500$ days $\frac{\pi_W\|_{\text{per}}}{\pi_W\|_{\text{CP}}} > 1.5$ $\frac{\frac{\pi_W}{\pi_P}\|_{\text{per}}}{\frac{\pi_W}{\pi_P}\|_{\text{CP}}} > 1.5$
⑩ Administration of OPG	OPG is administered to match 4 times the endogenous OPG level (see Table 1)	$R \searrow$ $B \searrow$ $C \searrow$ $C/B \searrow$ $T_{ss} < 500$ days $\frac{\pi_L\|_{\text{ref}}}{\pi_L\|_{\text{per}}} > 1.5$
⑪ Administration of RANKL	RANKL is administered to match 4 times the endogenous RANKL level (see Table 1)	$R \nearrow$ $B \nearrow$ $C \nearrow$ $C/B \nearrow$ $T_{ss} < 500$ days $\frac{\pi_L\|_{\text{ref}}}{\pi_L\|_{\text{per}}} > 1.5$

'ref' refers to the "state of reference", which is the unperturbed state, before a perturbation is applied. 'per' refers to the perturbed state in a given experiment. The objectives indicate the qualitative change that should be achieved by the system when it is going from the steady state of the unperturbed state to the steady state of the perturbed state. For example, $R \nearrow$ means that the density in responding osteoblasts at steady state should rise significantly when going from the unperturbed state to the perturbed state

optimization procedure. There are 18 fitting parameters for the PK models, 5 for PTH, 5 for the anti-RANKL antibody and 8 for the anti-sclerostin antibody. The values for these parameters, determined from the optimization procedure, are recapitulated in Table 3. In addition, there are 2 PK parameters that were obtained from the literature

Table 6 These are the steady-state values of the model variables for parameters values given in Tables 2, 3 and 4

Symbol	Unit	Value of reference	Description
B	pM	7.284×10^{-6}	Active osteoblasts (see Eq. (1))
C	pM	1.26×10^{-6}	Active osteoclasts (see Eq. (1))
R	pM	9.963×10^{-6}	Responding osteoblasts (see Eq. (1))
$K \circ L$	pM	5.979×10^{-7}	RANK-RANKL complexes (see Eq. (26))

These values are the result of experiment 1 of Table 5. When the system is at steady state, the overall bone balance is neutral, meaning that there is no excess or deficit of bone. This state is called state of reference, or healthy state

(Table 4), the bioavailability after subcutaneous injection of PTH(1–34) (Clausen 2009), and of the anti-RANKL antibody denosumab (Sutjandra et al. 2011).

2.4 Model Simulations

The bone model presented in Sect. 2.2 was solved numerically using the parameter values of reference presented in Tables 2, 3 and 4. For these parameter values, the steady-state values for the model variables are indicated in Table 6. At this particular steady state, labeled the state of reference, the overall bone balance is neutral, meaning that there is no excess or deficit of bone. The state of reference is also called the healthy state, as opposed to disease states which we discuss in Sect. 4. The steady-state values for the state of reference were estimated from the first experiment of Table 5 during parameter estimation (see Sect. 2.3). Although one of the objectives is not strictly respected as $\max(R, B, C) = 9.963 \cdot 10^{-6} < 10^{-5}$, the difference between the obtained value and the objective is marginal, and not significant when appreciated within all the results of the optimization procedure. Interestingly, the level of RANK-RANKL complexes at steady state is about 8.2% of the level of active osteoblasts. This indicates that, at steady state, a maximum of 8.2% of active osteoblasts are involved in inducing osteoclasts maturation/activation through cell-to-cell contact with osteoclast precursors. That is assuming only one RANK-RANKL connection is enough for osteoclast activation. If more than one connection is necessary (which is likely), the proportion of active osteoblasts involved in osteoclast activation in the resting state (the reference state) would be even lower.

The remaining 10 experiments proposed in Table 5 are also simulated as shown in Figs. 3 and 4. Figure 3a, d, g corresponds to experiments in Table 5 where bone cells are added to the system at 1/8th of the steady-state level per day. The administration of cells starts at day 20 and stops at day 170, after a new steady state is reached. In these graphs, bone cell levels are normalized with respect to their value at steady state. This way, it is easier to assess relative changes in cell level and easier to see if the applied perturbation is making the system anabolic (making new bone)—when the osteoblast curve is higher than the osteoclast curve, or catabolic (losing bone)—when the osteoclast curve is higher than the osteoblast curve. We see that all objectives in Table 5 for these 3 experiments are well matched.

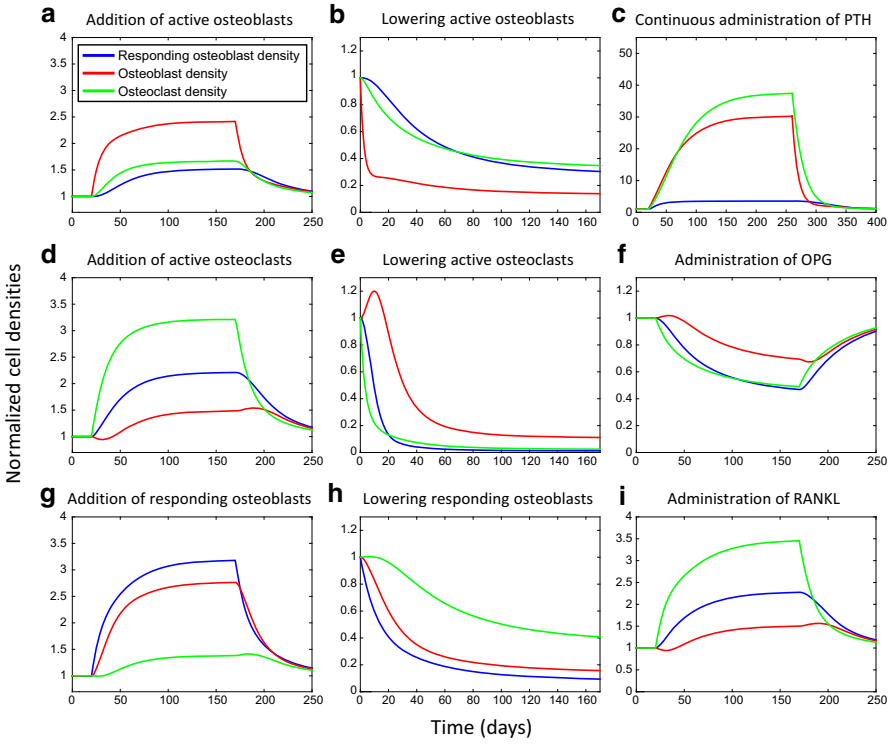

Fig. 3 Change in cell densities after perturbations are applied. These graphs are simulations of experiments 2–8, 10 and 11 of Table 5, as the graphs titles indicate. As indicated in the legend, the colored curves represent cell densities normalized to their respective steady-state value (which is the result of experiment 1 of Table 5). Normalizing concentrations makes it easier to compare relative changes of each cell type, and to determine if the overall contributions of osteoblasts and osteoclasts leads to bone formation (red curve higher than green curve) or bone resorption (green curve higher than red curve). In graphs **a**, **d**, **g**, **f** and **i**, perturbation in the experiment starts at day 20 and stops at day 170. In graphs **b**, **e** and **h**, perturbation starts at $t = 0$ and lasts for the duration of the experiment. In graph **c**, perturbation starts at day 20 and stops at day 260 (Color figure online)

In Figs. 3b, e, h, the opposite experiments are performed, where either the rate of elimination/death of bone cells is increased and/or the rate of differentiation is decreased, lowering the cell populations. In these cases, the perturbation starts at $t = 0$ and is sustained until the end of the experiment. Again, all objectives for these three experiments are well matched.

2.4.1 Continuous PTH, RANKL and OPG

Simulations of the 8th experiment in Table 5 are shown in Fig. 3c. In this experiment, PTH is administered at a constant rate that is 4 times the endogenous rate of PTH synthesis, leading to plasma PTH levels symptomatic of hyperparathyroidism. The effect is a net increase in osteoclasts as well as in osteoblasts, with an overall catabolic action, as it has been reported experimentally (Gogakos et al. 2009; Kramer

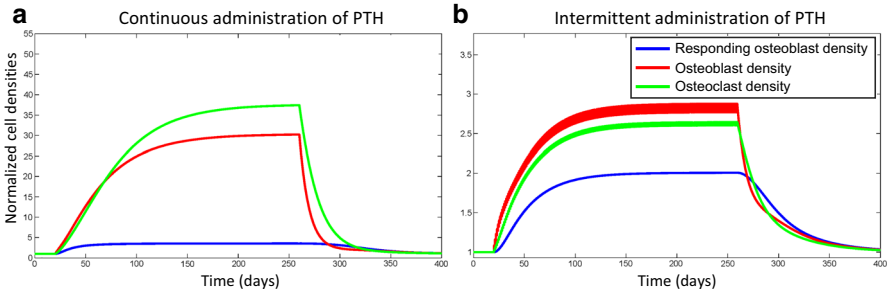

Fig. 4 Bone cell densities after continuous vs. intermittent administration of PTH. Graph **a** is the same as Fig. 3c, which corresponds to simulation of experiment 10 of Table 5. Graph **b** is a simulation of experiment 11 of Table 5. In both cases, the perturbation (i.e., administration of PTH, either continuous, graph **a**, or intermittent, graph **b**) starts at day 20 and stops at day 260. As in Fig. 3, the colored curves represent cell densities normalized to their respective steady-state value. Because cell densities are normalized, we can determine upfront if the applied perturbation leads bone formation (red curve higher than green curve) or bone resorption (green curve higher than red curve). Here you see that continuous infusion of PTH, at levels typical of hyperparathyroidism, leads to bone resorption, whereas intermittent administration of PTH, at 20 μg of teriparatide per day (injection), leads to bone formation (Color figure online)

et al. 2010). In contrast, responding osteoblasts do not rise as much. This is exactly what is seen clinically where PTH seems to decrease proliferation of less mature osteoblasts but increases differentiation of osteoblasts (Khosla et al. 2008). It has also been observed that during sustained exposure to high level of PTH, there is a clear temporal sequence where osteoblasts are stimulated first before osteoclasts catch up and outnumber the population of osteoblasts, leading to bone resorption (Canalis et al. 2007a). This is recapitulated in our model where the osteoblasts are stimulated first, and shortly followed by the osteoclasts. Figure 3f, i corresponds to experiments 10 and 11 of Table 5, with administration of OPG and RANKL, respectively. Again, the objectives for these experiments are well matched by the simulations.

2.4.2 Intermittent PTH

In Fig. 4, we show simulations comparing continuous (4a), and intermittent (4b), administration of PTH. In the case of continuous administration of PTH, the simulation is the same as the one shown in Fig. 3c, where the goal was to simulate conditions of hyperparathyroidism. In contrast, in the case of intermittent administration of PTH, the goal was to simulate the typical bone forming therapy based on daily injection of 20 μg teriparatide. Intermittent PTH treatment leads to an increase in both osteoblasts and osteoclasts with a balance in favor of bone formation, in agreement with observations (Gogakos et al. 2009; Kramer et al. 2010). Looking at the active osteoblast curve in Fig. 4b, you see that the curve is fluctuating at high frequency. This is the daily fluctuation of PTH dosing. The fluctuations of PTH are most visible on active osteoblasts because the action of PTH is most direct through the Wnt-SOST pathway. In reality, more complex trafficking and signaling mechanisms, not included in the model, dampen the fluctuations of the PTH signal. Already, we see that fluctuations of osteoclasts are much lower because the RANK-RANKL-OPG pathway is also

involved. Similarly, the responding osteoblasts are not visibly fluctuating because of the additional effect of the TGF-β pathway.

The model can differentiate between different dosing regimens of PTH, generating completely opposite bone formation/resorption patterns, as is observed in the clinics (Gogakos et al. 2009). This would indicate that the mechanism for differential responses to PTH dosing is part of the core regulatory system of bone remodeling, and is a consequence of the different PTH activation kinetics of the RANK-RANKL-OPG pathway and the Wnt-SOST pathway, as explained earlier in Sect. 2.1.

3 PK Models

3.1 PTH (1–34)

The only currently available anabolic treatment for osteoporosis is parathyroid hormone (PTH) when administered intermittently (e.g., one subcutaneous injection a day) (Hammerle et al. 2012). The therapeutic form of PTH is a fragment of the endogenous full-length PTH(1–84), for which the binding sequence has been conserved. It is often noted as PTH(1–34), and called teriparatide or Forteo. The molecular mass of PTH(1–34) is about 4.1 kDa (Clausen 2009; Sigma-Aldrich 2008), so 20 μg of PTH(1–34) is 4860 pmol. By comparison, PTH(1–84) has a molecular mass of 9.4 kDa (Ishibashi et al. 1993).

In order to test human dosing of PTH with the model, we need a pharmacokinetic model for PTH(1–34) calibrated on human data. We searched the literature for PK data of PTH(1–34) in human. We found eight studies reporting plasma concentration of PTH(1–34) after subcutaneous injection, and one study after intravenous injection (Chu et al. 2007; Daddona et al. 2011; Fraher et al. 1995; Hammerle et al. 2012; Lindsay et al. 1993; Pfutzner et al. 2003). These data are plotted in Fig. 5, and were used to calibrate a pharmacokinetic model for PTH(1–34).

The structure of the PK model for PTH(1–34) is shown in Fig. 6. It is a 2-compartment model for the systemic distribution with central elimination and first-order absorption from the subcutaneous site of injection. It is the minimal model which best matches the data in Fig. 5. The bioavailability of PTH(1–34) after subcutaneous injection is about 95% (Clausen 2009). Subcutaneous and intravenous data were fitted simultaneously using the same PK model. In the fitting procedure, more weight was assigned to the subcutaneous data than the intravenous data to account for the fact that the concentration curve after subcutaneous injection (Fig. 5a) is based on many more patients than the concentration curve after intravenous injection (Fig. 5b). That explains the difference between the model curve and the data points in Fig. 7b, since the model aims to capture the average PK in a healthy population and the IV data are only based on 1 study with 10 patients. Moreover, high variability is observed in the PK of PTH(1–34) between patient-to-patient and even study-to-study (Fig. 5a). Another explanation would be some nonlinearity in the PK at higher concentration, as in Fig. 5b. Nonetheless, the model captures well the average PK in a larger population, after subcutaneous injection (Fig. 7a).

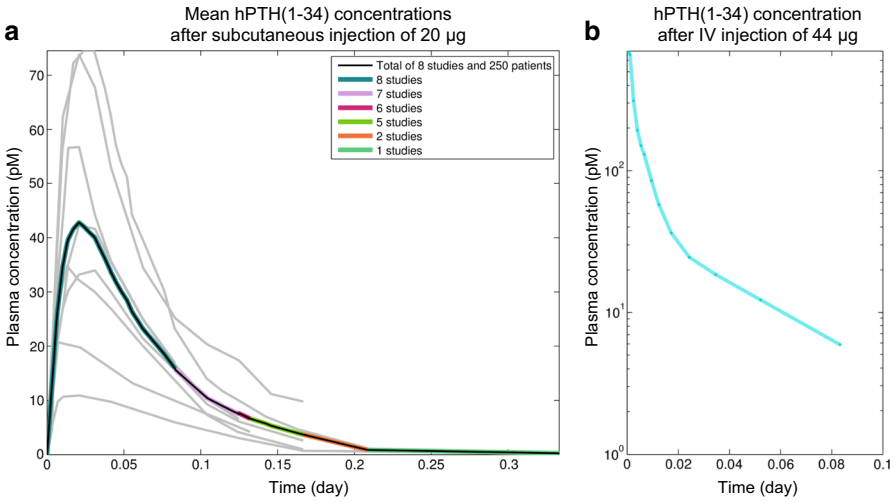

Fig. 5 **a** Mean concentrations of human PTH(1–34) after subcutaneous injection of 20 µg of PTH(1–34). 8 studies are displayed in gray. Not all studies were dosed at 20 µg. But all PK curves were normalized at 20 µg assuming the pharmacokinetics of PTH(1–34) is linear at that concentration range. Each study (each gray curve) is the mean of approximately 30 patients. You see that the variability is quite high. The black curve is the arithmetic mean of all the studies, and the colored segments indicate the number of studies contributing to the mean. The black curve is the data we used for model development and model calibration. **b** Mean concentration of human PTH(1–34) after intravenous injection of PTH(1–34) (Color figure online)

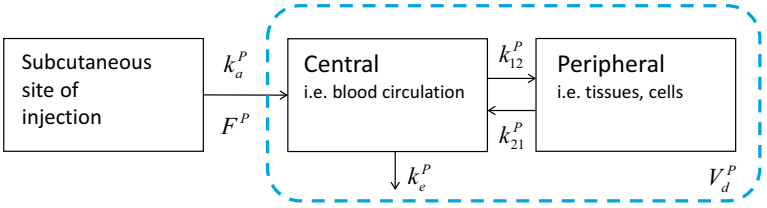

Fig. 6 Pharmacokinetic model for hPTH(1–34). We found the most appropriate structure was a 2-compartment model with central elimination $\boldsymbol{k_e^P}$ and first-order absorption $\boldsymbol{k_a^P}$ from the subcutaneous site of injection. Bioavailability after subcutaneous injection is $\boldsymbol{F^P}$, which is about 95% (Clausen 2009). The volume of distribution is $\boldsymbol{V_d^P}$

3.2 Anti-RANKL Antibody-Denosumab

Denosumab is an anti-RANKL antibody, approved in the US market for post-menopausal women with osteoporosis (Lacey et al. 2012). The molecular mass of denosumab is about 147 kDa (Amgen 2010), so 1 mg of denosumab is 6905 pmol.

As for PTH, we need a pharmacokinetic model of denosumab calibrated on human data to test the effect of realistic human dosing of denosumab with the model. We found a number of PK studies of denosumab in the literature which we can use for developing a pharmacokinetic model. In most of these studies, the drug was administered by subcutaneous injection. The pharmacokinetics of denosumab is not linear with dose

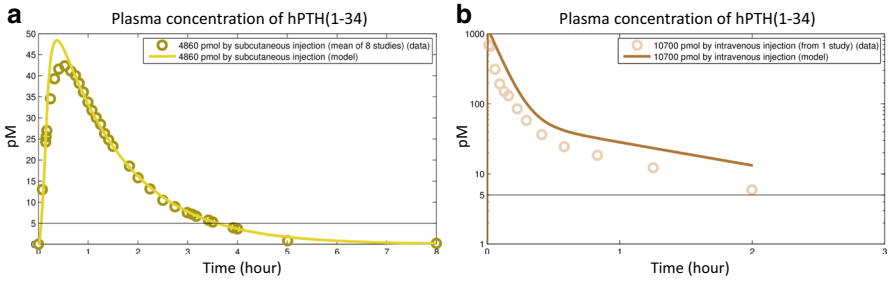

Fig. 7 **a** PK data of PTH(1–34) and model curve after subcutaneous injection of 20 μg of PTH(1–34). **b** PK data of PTH(1–34) and model curve after intravenous injection of 44 μg of PTH(1–34) (Color figure online)

because of target-mediated degradation of the antibody. So PK studies cannot be averaged all together like we did for PTH; however, concentration curves may be averaged from two different studies if the dose used is the same. We were able to collect enough PK data from the literature at four different doses in healthy patients: 7 mg, 20 mg, 65 mg and 200 mg (Bekker et al. 2004; Block et al. 2012; Gibiansky et al. 2012; Kumagai et al. 2011; Sutjandra et al. 2011; Yonemori et al. 2008). These data are shown in Fig. 8. The mean concentration curves of the four doses of reference were plotted again on the same graph in Fig. 9a for direct comparison. We see that denosumab gets eliminated faster at smaller concentration. This is because the naked antibody has different elimination rate than the complexed antibody.

The structure of the model for denosumab is shown in Fig. 10a. It is a 1-compartment model with target-mediated degradation, central elimination for both the naked antibody and the complexed antibody, and first-order absorption from the subcutaneous site of injection. Denosumab PK models with similar compartment structure have been used by other authors (Scheiner et al. 2014). The reported bioavailability of denosumab after subcutaneous injection is about 64% (Sutjandra et al. 2011). Based on the structure of the model in Fig. 10a, the equation for αL is

$$\frac{\mathrm{d}\alpha L}{\mathrm{d}t} = P^{\alpha L}(t) - k_e^{\alpha L} \cdot \alpha L - k_e^{\alpha L \circ L} \cdot \alpha L \circ L, \tag{37}$$

where $P^{\alpha L}(t)$ represents the external administration of denosumab (it is either a bolus in case of IV injection or a first-order absorption in case of subcutaneous injection), and assuming that the binding of the antibody with its target equilibrates faster than the other kinetics. Injecting (33) into (37), we get

$$\frac{\mathrm{d}\alpha L}{\mathrm{d}t} = P^{\alpha L}(t) - \left(\frac{k_e^{\alpha L \circ L}}{k_D^{\alpha L}} \cdot L + k_e^{\alpha L} \right) \cdot \alpha L, \tag{38}$$

where L is given by (36) and $K \circ L$ (in L) is given by (26). You see that the PK model for denosumab depends on L, a variable of the biological model. The biological model is calibrated first and independently from the PK model. So, on one hand, if the bone model would not be a good model, or if it would not be calibrated properly, it might

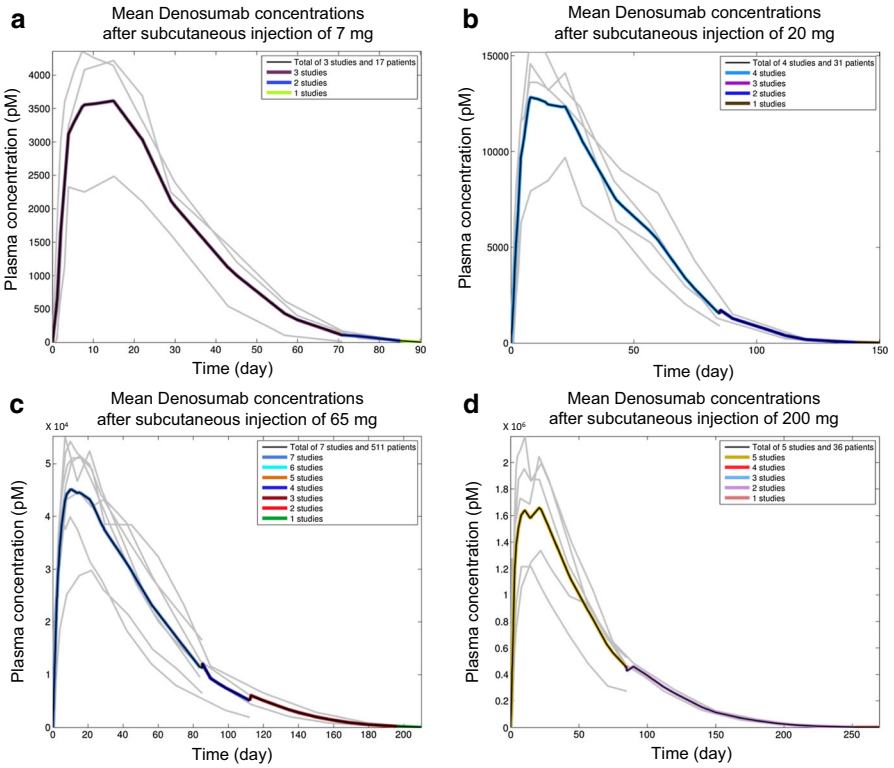

Fig. 8 Plasma concentrations of denosumab in healthy patients after subcutaneous injection of four different doses. 7 mg in (**a**) 20 mg in (**b**), 65 mg in (**c**) and 200 mg in (**d**). Each concentration curve (in black with colored segments) corresponds to the average of many studies performed at the same dose (gray curves). When a dose used in a study was different but close to one of the 4 reference doses (for example, 60 mg instead of 65 mg), the concentration curve was normalized with respect to the reference dose, assuming local linearity around the reference dose (Color figure online)

not be possible to achieve a good fit with the PK model, since it depends on the bone model. On the over hand, if the bone model is realistic and well calibrated, it should make the PK model better due to the added mechanistic attributes it would provide.

The model calibration was done using data in Fig. 9a. Parameter optimization was done using all data sets at the same time; the results are shown in Fig. 11. You see that the model has well captured the nonlinearity with concentration caused by target-mediated degradation.

3.3 Anti-sclerostin Antibody-Romosozumab

Romosozumab is an anti-sclerostin antibody, currently undergoing Phase 3 clinical trials for postmenopausal osteoporosis (Li et al. 2009). The molecular mass of romosozumab is about 145.9 kDa (Amgen 2009). So 1 mg of romosozumab is 6854 pmol.

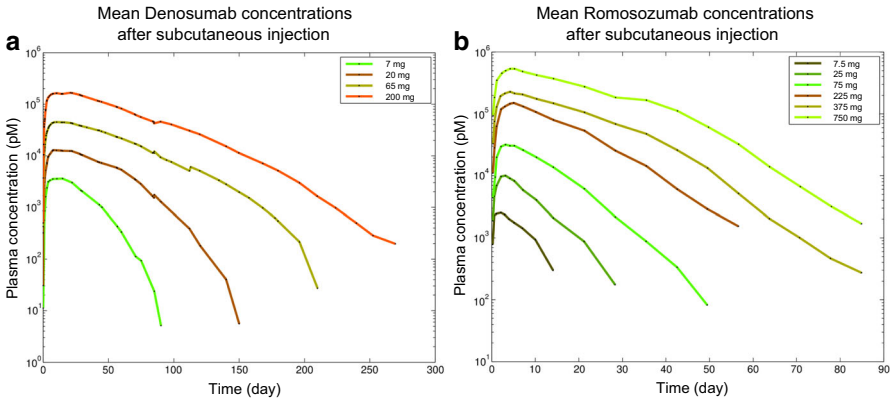

Fig. 9 a Same mean denosumab concentration curves as in Fig. 8 but plotted on the same graph for direct comparison. **b** Plasma concentration of romosozumab in healthy patients after subcutaneous injection of 6 different doses (Padhi et al. 2011) (Color figure online)

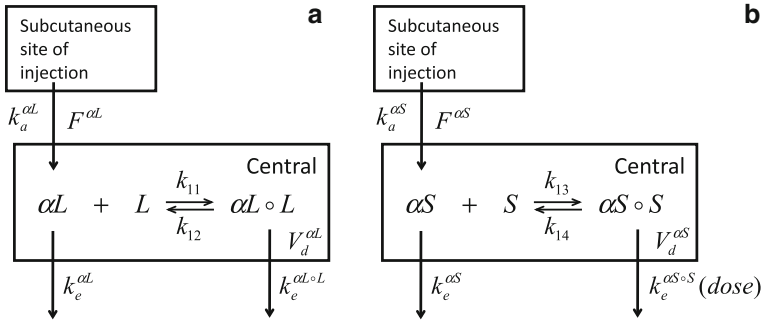

Fig. 10 a Pharmacokinetic model for denosumab. It is a 1-compartment model with central elimination for both the naked antibody and the complexed antibody ($\boldsymbol{k_e^{\alpha L}}$ and $\boldsymbol{k_e^{\alpha L \circ L}}$), and first-order absorption $\boldsymbol{k_a^{\alpha L}}$ from the subcutaneous site of injection. Bioavailability after subcutaneous injection is $\boldsymbol{F^{\alpha L}}$, which is about 64% (Sutjandra et al. 2011). The volume of distribution is $\boldsymbol{V_d^{\alpha L}}$. **b** The pharmacokinetic model for romosozumab has a similar structure to the PK model for denosumab. The main difference is a dose-dependent elimination rate of the complexed antibody in the case of romosozumab, indicating saturation of the degradation process. Bioavailability after subcutaneous injection is $\boldsymbol{F^{\alpha S}}$, which was estimated to about 69%. The volume of distribution is $\boldsymbol{V_d^{\alpha S}}$

We developed a human pharmacokinetic model of romosozumab to test the effect of an anti-sclerostin antibody on the bone cells dynamics after realistic dosing of the drug. We found only one study with concentration data in healthy patients after administration of romosozumab at 6 different doses (Padhi et al. 2011). These data are displayed in Fig. 9b and will be used for model calibration. The structure of the model is similar to the PK model of denosumab (see Fig. 10b). Based on that structure, the equation for αS is

$$\frac{\mathrm{d}\alpha S}{\mathrm{d}t} = P^{\alpha S}(t) - k_e^{\alpha S} \cdot \alpha S - k_e^{\alpha S \circ S} \cdot \alpha S \circ S, \tag{39}$$

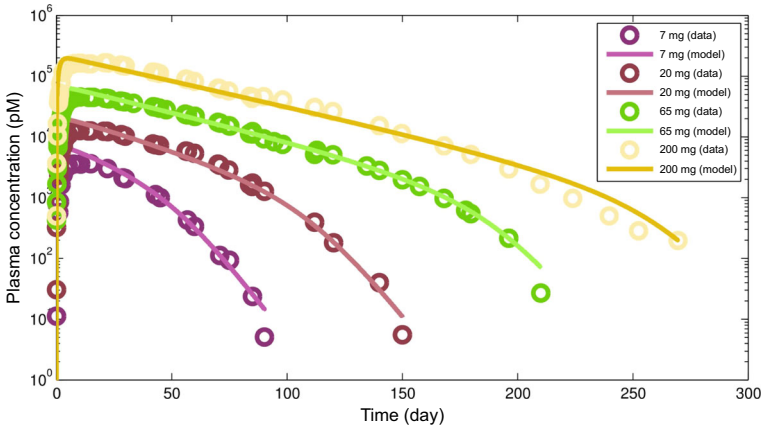

Fig. 11 Best fit of the denosumab PK model over the PK data presented in Fig. 9a (Color figure online)

where $P^{\alpha S}(t)$ represents the external administration of romosozumab (it is either a bolus in case of IV injection or a first-order absorption in case of subcutaneous injection). Assuming that the binding of the antibody with its target equilibrates faster than the other kinetics, we get

$$\frac{\mathrm{d}\alpha S}{\mathrm{d}t} = P^{\alpha S}(t) - \left(\frac{k_e^{\alpha S \circ S}}{k_D^{\alpha S}} \cdot S + k_e^{\alpha S} \right) \cdot \alpha S. \tag{40}$$

Injecting the expression for S from the bone model (14) into (40), we get

$$\frac{\mathrm{d}\alpha S}{\mathrm{d}t} = P^{\alpha S}(t) - \left(\kappa_2 \cdot \frac{\kappa_1}{\alpha S + \kappa_1} \cdot \left(\frac{1}{\pi_P} + i_S \right) + k_e^{\alpha S} \right) \cdot \alpha S, \tag{41}$$

where $\kappa_2 = k_e^{\alpha S \circ S} \cdot K_D^S$ and κ_1 is given in (15). i_S and K_D^S are defined in Sect. 2.2. Similarly to denosumab, the PK model for romosozumab is connected to the bone model through π_P (defined in (24)), but also through κ_1, which is calibrated from the bone model (independently from the PK model).

We found that the degradation rate of the complexed antibody $k_e^{\alpha S \circ S}$ is dose-dependent. When doing model calibration, the parameter κ_2 was allowed to be different at different doses whereas the other parameters were held constant for all doses (since $k_e^{\alpha S \circ S}$ is lumped into κ_2). The result of the parameter optimization for κ_2 is shown in Fig. 12. These data strongly indicate a saturation process in the degradation of the complexed romosozumab. No other parameters were found to depend on dose for the dose range in Fig. 9b. To represent the dose-dependency of κ_2 in the model, we use a decreasing exponential function of the form

$$\kappa_2(\text{dose}) = \kappa_2^0 \cdot e^{-\left(\ln(2)/\kappa_2^{50}\right) \cdot \text{dose}} + \kappa_2^{\min}, \tag{42}$$

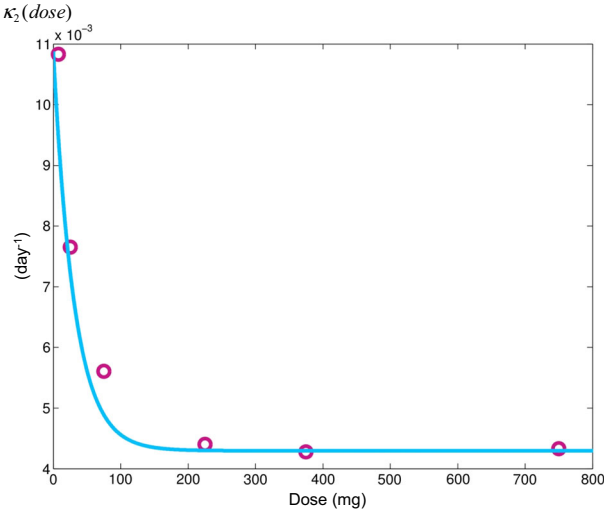

Fig. 12 Degradation of the complexed romosozumab is dose-dependent. The data (red circles) are the best fit for κ_2 when allowed to take different values at different doses while the other parameters could not depend on dose. The trend of the data clearly indicates a saturation phenomenon of $k_e^{\alpha S \circ S}$ (which is lumped into κ_2) at increasing doses. The blue curve is a decreasing exponential function of the form $A \times e^{-b \cdot x} + C$ representing these data. Parameters A, b and C were optimized with the rest of the PK parameters. The result of the parameter estimation for the whole PK model can be seen in Fig. 13

where κ_2^0, $\kappa_2^{\min}$ and κ_2^{50} are constant parameters. κ_2^{50} being the dose leading to half saturation, meaning $\kappa_2\left(\kappa_2^{50}\right) = \frac{\kappa_2^0 + 2 \cdot \kappa_2^{\min}}{2}$. Best fit for $\kappa_2(\text{dose})$ is the blue curve in Fig. 12. Values found from parameter optimization are $\kappa_2^0 = 6.58 \cdot 10^{-3}\text{day}^{-1}$, $\kappa_2^{min} = 4.3 \cdot 10^{-3}\text{day}^{-1}$ and $\kappa_2^{50} = 21.75\text{mg}$ (or 149,075 pmol). 21.75 mg is a rather small dose, so for most therapeutic doses (>200 mg), the model is not dose-dependent. The result of parameter optimization for the whole PK model is shown in Fig. 13.

Parameter κ_1 in (15) depends also on $k_e^{\alpha S} \circ^S$. However, κ_1 is not dose-dependent in the model. The reason is that $k_e^{\alpha S \circ S}$ is much greater than k_{14} in the expression of κ_1, so $k_e^{\alpha S \circ S}$ cancels out in the ratio. For that matter, κ_1 could be approximated as $\kappa_1 = \frac{k_e^S}{k_{13}}$.

4 Simulation of Bone Diseases

Osteoporosis is a disease, characterized by a decreased bone mass and density, with many different causes. There are two main categories of osteoporosis, primary and secondary. Primary osteoporosis is an age-related bone loss, due to the aging of the cellular processes of bone remodeling. Primary osteoporosis may be further classified as type 1 and type 2. Type 1 refers to postmenopausal osteoporosis and is caused by a decrease in estrogen production after menopause. Type 2 refers to senile osteoporosis. This type of osteoporosis is seen in both men and women, with increasing prevalence at older age. Secondary osteoporosis refers to patients with osteoporosis not caused

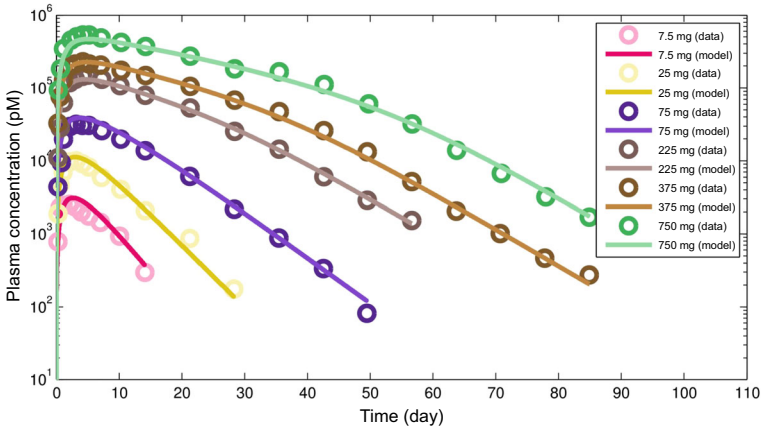

Fig. 13 Best fit of the romosozumab PK model over the PK data presented in Fig. 9b (Color figure online)

by menopause or aging, and usually results from other diseases or conditions predisposing to bone loss (Lorentzon and Cummings 2015). In this paper, we consider the two categories of primary osteoporosis and three typical conditions of secondary osteoporosis: glucocorticoid-induced osteoporosis, hyperparathyroidism and vitamin D deficiency. There are many other conditions leading to secondary osteoporosis but these three are common examples of secondary osteoporosis.

Our goal is to simulate these five osteoporotic diseases with the model; they are summarized in Table 7. Then, in Sect. 5, we use the model to explore dosing regimens for monotherapy, or combination of therapies, against these diseases, based on the 3 treatments included in the model: intermittent PTH, administration of a RANKL antibody (denosumab), administration of a Sclerostin antibody (romosozumab). Although the diseases are most likely caused by more than one dysfunction, we tried to identify the main impairment that would be the signature of each disease. We did that for simplicity, but also because the full spectrum of all dysfunctions of each disease is, for the most part, unknown. Our goal, for the simulation of these diseases, is to capture qualitatively well the phenotype of each disease. We are not trying to represent the onset of the diseases or their progression in time.

Table 7 Five different types of osteoporosis are represented in the model. They are summarized in this table with their category of osteoporosis, the cause of each disease, the main biological or cellular process being impaired in each disease, and what is modified in the model to simulate each disease

Disease	Osteoporosis type	Cause	Main impaired process	Simulated in the model by
Postmenopausal Osteoporosis	Primary Type 1	Estrogen deficiency	Decreased OPG production	$\uparrow K_D^O$
Senile Osteoporosis	Primary Type 2	Senescence	Decreased TGF-β production	$\uparrow C_{50}$
Glucocorticoid-Induced Osteoporosis	Secondary	Glucocorticoid excess	Decreased osteoblast progenitor differentiation	$\downarrow D_R$
Hyperparathyroidism	Secondary	Over activity of parathyroid gland	Increased PTH synthesis	Adding continuous PTH in central compartment
Vitamin D Deficiency	Secondary	Vitamin D insufficiency		

4.1 Postmenopausal Osteoporosis

Postmenopausal osteoporosis is thought to be caused by estrogen deficiency after menopause, which leads to a decrease in OPG production by osteoblastic cells (Sipos et al. 2009). In the model, the disease is simulated by increasing K_D^O in Eq. (36). K_D^O was multiplied by a factor ranging in the interval [1.2, 2000], depending on the disease severity (the variation was made on a log scale).

4.2 Senile Osteoporosis

Senile osteoporosis is characterized by a gradual age-related alteration of osteoblast differentiation and functions. An important consequence of this condition is a decrease in TGF-β production by osteoblasts during bone formation (Fromigue et al. 2004; Kassem and Marie 2011; Moerman et al. 2004). In the model, this is represented by increasing C_{50} in Eq. (2). C_{50} was multiplied by a factor ranging in the interval [1.15, 1.65], depending on the disease severity.

4.3 Glucocorticoid-Induced Osteoporosis

Glucocorticoid-induced osteoporosis is arising from the chronic use of glucocorticoid medicines that are being prescribed for their potent anti-inflammatory and immunosuppressive effects. One of the main detrimental effects of these drugs is a reduction in osteoblast proliferation, such as less mature osteoblasts (Mazziotti et al. 2006; O'Brien et al. 2004; Weinstein 2001). In the model, this effect is simulated by decreasing parameter D_R in Eqs. (1). D_R was multiplied by a factor ranging in the interval [0.65, 0.9], depending on the disease severity.

4.4 Hyperparathyroidism

Hyperparathyroidism is caused by the overactivity of the parathyroid glands, leading to an increase in PTH synthesis. To simulate this disease in the model, we simply added a continuous supply of PTH in the central compartment at levels that would raise PTH blood concentration in the range of hyperparathyroidism (i.e., 4 times normal PTH levels or higher).

4.5 Vitamin D Deficiency

Osteoporosis due to vitamin D deficiency is caused by insufficient levels of vitamin D. PTH secretion and vitamin D levels are connected through feedback mechanisms of the calcium homeostasis (Bergwitz and Jüppner 2010). For that reason, vitamin D deficiency also leads to increased PTH synthesis (Holick 2007). So this disease is also simulated in the model by raising PTH levels in the central compartment. This was done by infusing PTH at $1.7 \cdot 10^4$ pM/day.

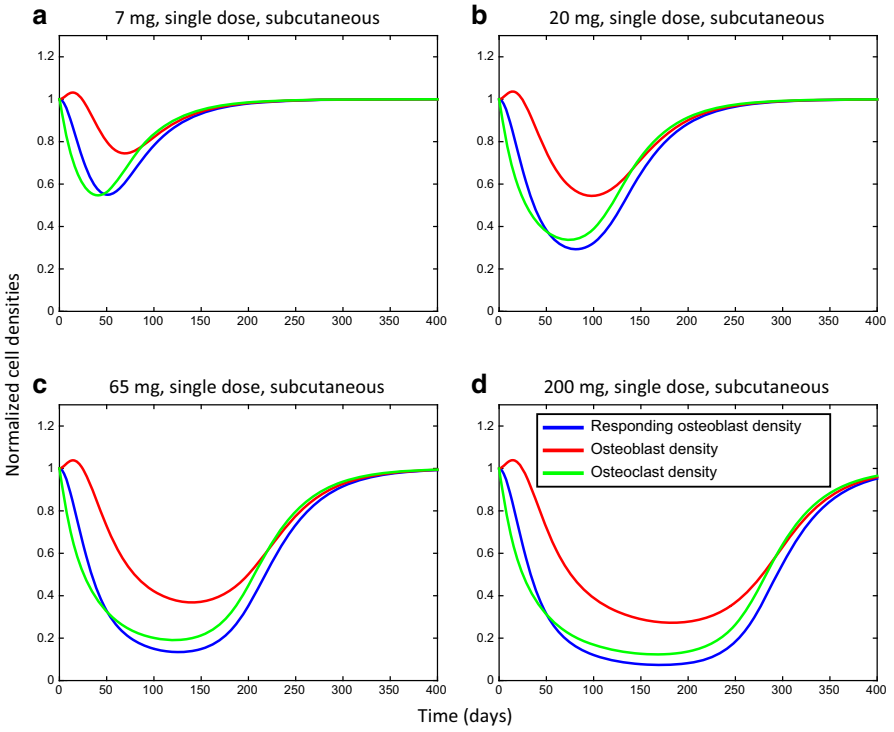

Fig. 14 Change in cell densities after administration of denosumab. These graphs are simulations of bone cell densities after subcutaneous injection of denosumab at 4 different doses. Doses are indicated in the title of each graph; they are the same doses used in the PK studies in Fig. 9a. As in Figs. 3 and 4, cell densities are normalized with respect to their value at steady state (drug-free state) (Color figure online)

5 Therapies

As mentioned, our goal is to explore dosing regimens based on the 3 treatments represented in the model, as monotherapy or combination therapies. To demonstrate these therapies, we plot in Fig. 14 the bone cell densities after injection of 4 doses of denosumab (same doses used in the PK studies in Fig. 9a), and we plot in Fig. 15 the bone cell densities after injection of 6 doses of romosozumab (same doses used in the PK studies in Fig. 9b). Bone cell densities after a typical intermittent PTH treatment are shown in Fig. 4b.

We see that both treatments by a RANKL antibody (denosumab) and a sclerostin antibody (romosozumab) lead to an overall effect in favor of bone formation (since the active osteoblast curve is higher that the osteoclast curve during treatment). However there is an important difference between the two treatments. On the one hand, the RANKL antibody treatment leads to a lower bone turnover compared to the drug-free state (lower bone cell densities), which is what is observed in denosumab clinical trials (Bone et al. 2008, 2011; Kendler et al. 2010). On the other hand, the sclerostin antibody treatment leads to a higher bone turnover compared to the drug-free state. It

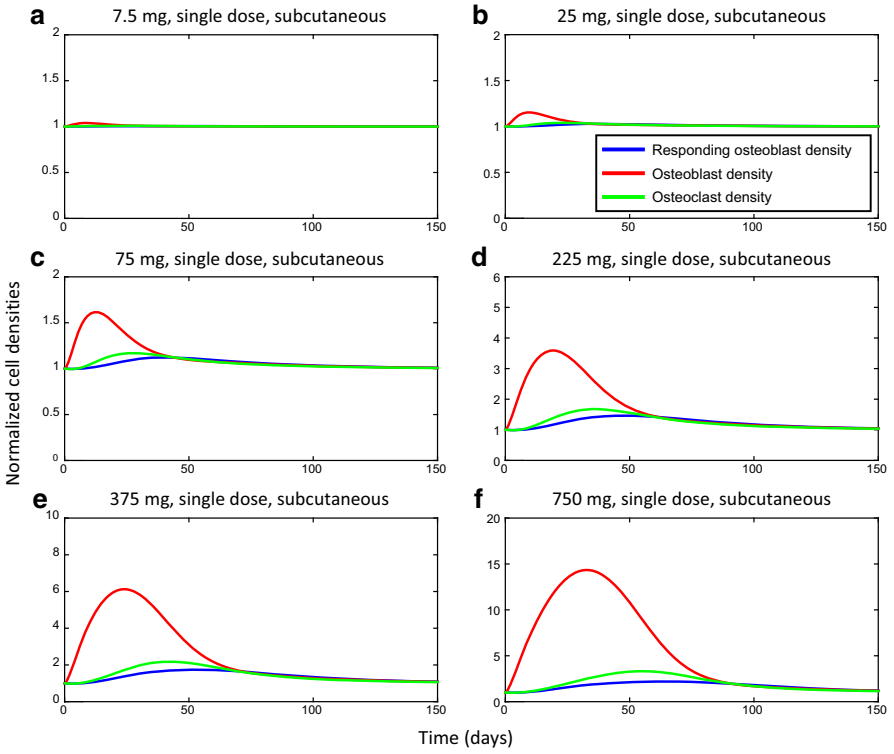

Fig. 15 Change in cell densities after administration of romosozumab. These graphs are simulations of bone cell densities after subcutaneous injection of romosozumab at 6 different doses. Doses are indicated in the title of each graph; they are the same doses used in the PK studies in Fig. 9b. As in Figs. 3 and 4, cell densities are normalized with respect to their value at steady state (drug-free state) (Color figure online)

is an interesting difference that we want to exploit in testing combination therapies of the two antibodies in the next section. Another interesting property of the treatment by sclerostin antibody is that it leads to a much higher raise in osteoblasts than in osteoclasts, as if perturbing the Wnt-SOST pathway by the action of the sclerostin antibody would attenuate the coupling between osteoblasts and osteoclasts (this is better seen in Fig. 16b). For comparison, osteoblasts and osteoclasts are more tightly coupled during intermittent PTH treatment, in the case of a bone turnover increasing therapy (as seen in Fig. 4b), or during denosumab treatment, in the case of a bone turnover lowering therapy (as seen in Fig. 16b). It was reported in clinical trials that the administration of romosozumab leads to a significant increase in bone formation biomarkers, whereas there was no clear effect on bone resorption biomarkers (Lewiecki 2011). Looking more closely at romosozumab clinical trials, we see that bone resorption biomarkers initially decrease before they start to rise slightly (Padhi et al. 2011). This is very similar to what we observe in the model simulations. Looking at graphs c-f in Fig. 15, we see that the osteoclast curve starts by decreasing very briefly before moderately increasing.

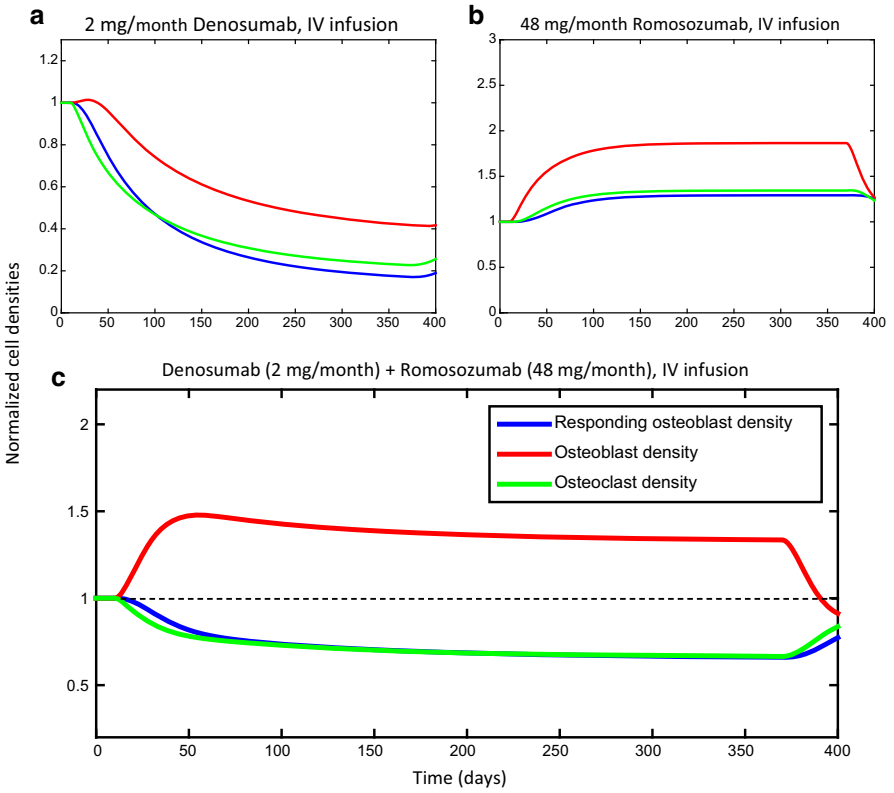

Fig. 16 Mono or combination therapies of denosumab and romosozumab by IV infusion. These graphs are simulations of bone cell densities after IV infusion of denosumab at 2 mg per month for 12 months, starting at day 10 and stopping at day 370 (**a**); or IV infusion of romosozumab at 48 mg per month for 12 months, starting at day 10 and stopping at day 370 (**b**); or IV infusion of both denosumab and romosozumab at same infusion rates and dosing schedule as in cases 'a' and 'b'(**c**). As in Figs. 3 and 4, cell densities are normalized with respect to their value at steady state (drug-free state) (Color figure online)

5.1 Combination Therapies

As mentioned, denosumab and romosozumab lead to an overall effect in favor of bone formation, either at a lower or higher bone turnover. We argue that, a lower bone turnover—in the case of denosumab (Fig. 16a), or a higher bone turnover—in the case of romosozumab (Fig. 16b), might not be an ideal bone formative therapy on the long term. We think a lower bone turnover might lead to a slower rate of bone deposition, and higher bone turnover might lead to a too fast, uncontrolled bone deposition pattern. So we believe that a neutral bone turnover, similar to the one in the healthy state, might be preferable. We see that, by combining denosumab with romosozumab at a proper dose ratio, we can achieve bone formation with a neutral bone turnover, as shown in Fig. 16c. Having a continuous infusion of drug over 12 months is not realistic. So we did a similar simulation using a more realistic dosing regimen based on multiple subcutaneous injections (1 injection of denosumab every 4 months combined with

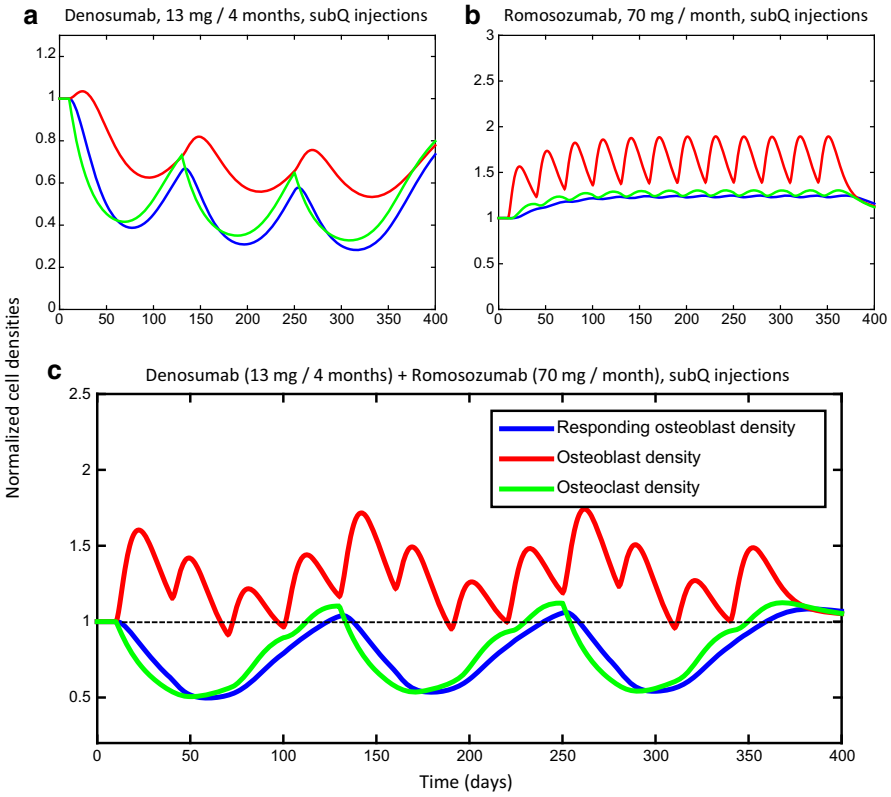

Fig. 17 Mono or combination therapies of denosumab and romosozumab by multiple subcutaneous injections. These graphs are simulations of bone cell densities after multiple subcutaneous injections of denosumab, with 1 injection of 13 mg every 4 months for 12 months (total of 3 injections), starting at day 10 and stopping at day 370 (**a**); or multiple subcutaneous injections of romosozumab, with 1 injection of 70 mg every month for 12 months (total of 12 injections), starting at day 10 and stopping at day 370 (**b**); or multiple subcutaneous injections of both denosumab and romosozumab at same dosing as in cases 'a' and 'b' (**c**). As in Figs. 3 and 4, cell densities are normalized with respect to their value at steady state (drug-free state) (Color figure online)

1 injection of romosozumab every month). The result of this simulation is shown in Fig. 17, where we see that it produces a similar outcome in terms of bone formation and bone turnover.

5.2 Exploring Dosing Regimens

In this section, we use the model to explore dosing regimens based on administration of intermittent PTH, denosumab or romosozumab to treat the osteoporotic diseases presented in Sect. 4. We did not find a situation where using intermittent PTH alone or in combination would be more favorable than another combination not using intermittent PTH. So, in the remaining, we only present combinations of denosumab and romosozumab.

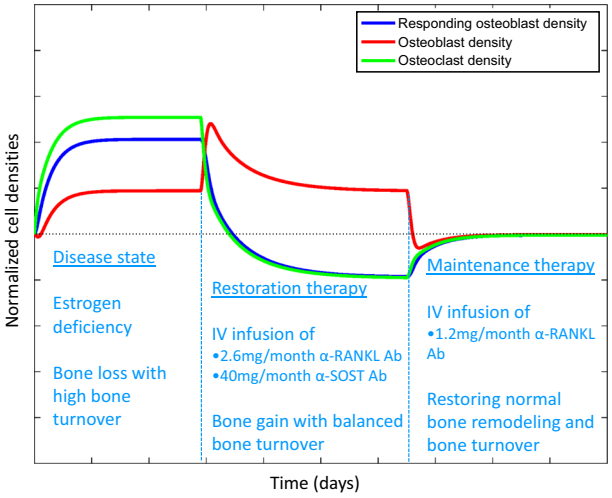

Fig. 18 Combination therapy using denosumab and romosozumab for postmenopausal osteoporosis (estrogen deficiency). We are showing simulations of bone cell densities with the model simulating bone regulation as in postmenopausal osteoporosis. Bone cell densities are normalized with respect to their value at steady state of the healthy state. Then a combination of denosumab and romosozumab is administered at a particular drugs ratio and dose as therapy. The goal of the restoration therapy is to achieve a positive balance in bone formation with a neutral bone turnover (as explain in "Exploring dosing regimens" section). The maintenance therapy is aiming at restoring a normal bone turnover and bone regulation as in a healthy subject (Color figure online)

For each disease, the treatment is made of three phases. The first phase is the "Disease state" phase, where we use the model to simulate the disease and let the system go to the disease steady state. The second phase is the "Restoration therapy" phase, where we inject a combination of denosumab and romosozumab at proper doses and ratio to achieve bone formation with a neutral bone turnover, as in Fig. 16c. During the therapy phases, the model is still simulating the disease state, so the medications are injected on top of the disease state. Finally, the third phase is the "Maintenance therapy" phase, where we inject a combination of denosumab and romosozumab with different doses and ratio to achieve bone cell densities of the healthy state (Table 6). The goal of the restoration therapy is to build up new bone in a patient with low bone mass density. When enough bone has been built, the maintenance therapy allows reestablishing normal bone remodeling processes for the duration of the disease. These three phases are demonstrated in Figs. 18, 19 and 20. The therapies proposed in Figs. 18, 19 and 20 are examples of adequate dosing regimens in the combination of denosumab and romosozumab for the disease type, disease severity, therapy types, and timing of therapy start simulated in these figures. Under different conditions, the optimal therapies might be different. According to the model, these therapies should lead to a better outcome in terms of bone health, assuming that bone density and bone quality is directly relatable to osteoblast and osteoclast numbers.

Postmenopausal osteoporosis leads to a significant increase in bone turnover in comparison to healthy subjects, with an increase in both bone formation and bone resorption biomarkers (Jabbar et al. 2011). Our model simulation of estrogen defi-

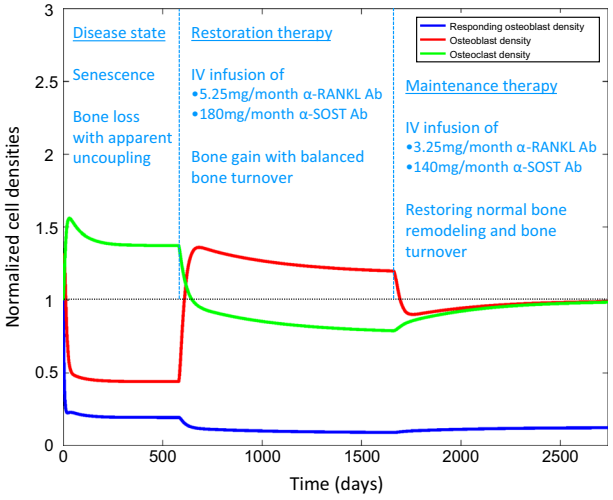

Fig. 19 Combination therapy using denosumab and romosozumab for senile osteoporosis. We are showing simulations of bone cell densities with the model simulating bone regulation as in senile osteoporosis. Bone cell densities are normalized with respect to their value at steady state of the healthy state. Then a combination of denosumab and romosozumab is administered at a particular drugs ratio and dose as therapy. The goal of the restoration therapy is to achieve a positive balance in bone formation with a neutral bone turnover (as explain in "Exploring dosing regimens" section). The maintenance therapy is aiming at restoring a normal bone turnover and bone regulation as in a healthy subject (Color figure online)

ciency shows the same behavior as we can see in Fig. 18. The identified combination to achieve a restoration therapy is 2.6 mg per month of denosumab with 40 mg per month of romosozumab. Then, maintenance therapy is achieved with 1.2 mg per month of denosumab, with no need of romosozumab.

Simulation of senile osteoporosis leads to a decrease in osteoblasts associated with an increase in osteoclasts, giving the impression of an apparent uncoupling of the bone cells, as seen in Fig. 19. Clinical studies show a decrease in bone mass, osteoblastogenesis and bone formation (Pietschmann et al. 2009), resulting from imbalance between bone resorption and bone formation at the bone remodeling unit (Vasikaran 2008). The identified combination for the restoration therapy is 5.25 mg per month of denosumab with 180 mg per month of romosozumab. The maintenance therapy requires 3.25 mg per month of denosumab with 140 mg per month of romosozumab.

Simulation of glucocorticoid-induced osteoporosis with the model results in decrease in both osteoblast and osteoclast levels, as seen in Fig. 20. Clinical evaluation of patients with glucocorticoid-induced osteoporosis indicates a decrease in bone formation and bone turnover in these patients compare to healthy subjects (Canalis et al. 2007b). We found that the combination to achieve a restoration therapy with this condition is 2.25 mg per month of denosumab with 225 mg per month of romosozumab. For the maintenance therapy, the combination is 0.56 mg per month of denosumab with 185 mg per month of romosozumab.

We notice that for senile osteoporosis and for glucocorticoid-induced osteoporosis, our combination therapies lead to a lower-than-normal level in responding osteoblast,

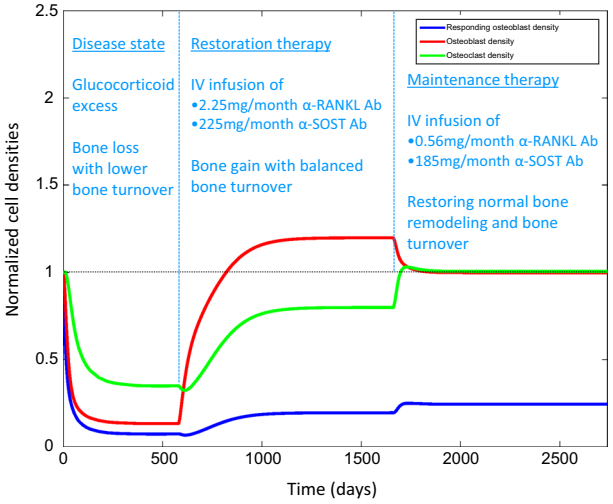

Fig. 20 Combination therapy using denosumab and romosozumab for glucocorticoid-induced osteoporosis. We are showing simulations of bone cell densities with the model simulating bone regulation as in glucocorticoid-induced osteoporosis. Bone cell densities are normalized with respect to their value at steady state of the healthy state. Then a combination of denosumab and romosozumab is administered at a particular drugs ratio and dose as therapy. The goal of the restoration therapy is to achieve a positive balance in bone formation with a neutral bone turnover (as explain in "Exploring dosing regimens" section). The maintenance therapy is aiming at restoring a normal bone turnover and bone regulation as in a healthy subject (Color figure online)

even for the maintenance therapy. In fact, the therapies increase the differentiation rate of responding osteoblasts so they do not accumulate much, and their level stays low. We do not know what could be the long term consequences of a lower level of responding osteoblasts, or if there would be any.

As for secondary osteoporosis due to hyperparathyroidism or vitamin D deficiency, and caused by a higher endogenous production of PTH, we could not identify any successful therapy based on denosumab, romosozumab, or intermittent PTH. Standard treatments for these two conditions involve vitamin D supplement in case of vitamin D deficiency, and partial or complete surgical removal of the parathyroid glands in case of hyperparathyroidism. Traditional osteoporosis medications, such as bisphosphonates, have been tried against these conditions, leading to only limited success (Mosekilde 2008). Our model confirms that (primary) osteoporosis medications are likely to be ineffective against hyperparathyroidism or vitamin D deficiency because they do not target the appropriate pathway. The model could be used to determine which pathway should rather be targeted for these two conditions; but this was not done here, although it was done in an earlier version of the model (Lemaire et al. 2004).

5.3 Precision Medicine

In this section, we show how the model was used to identify adequate ratio and doses of romosozumab and denosumab in function of the degree of severity of each

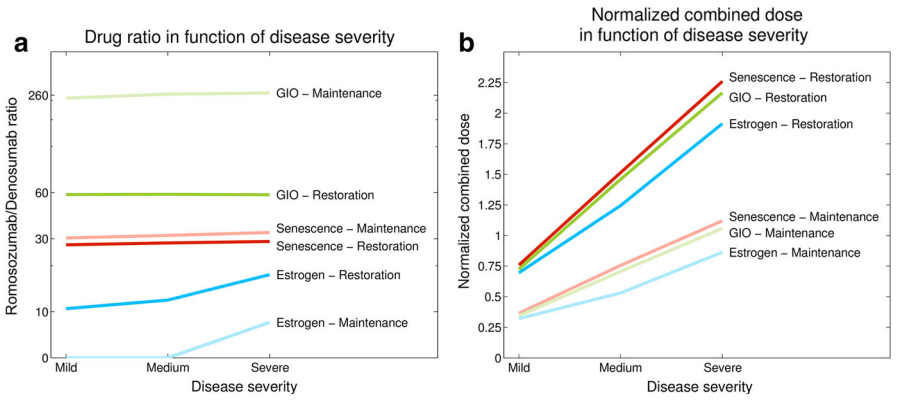

Fig. 21 These graphs show that the appropriate ratio of drugs and doses, in a combination of denosumab and romosozumab, could be different in every osteoporosis patient since it depends, at least, on the type of osteoporotic disease and the advancement of the disease (severity), as well as on the type of therapy being performed (Color figure online)

disease. The result of this analysis is summarized in Fig. 21. The severity of the disease was modulated by changing the value of the parameters in Table 7, leading to an increase or a decrease in the intensity of the main disease dysfunction. In the case of estrogen deficiency, severe postmenopausal osteoporosis was simulated by combining effects from lower estrogen as well as effects from senescence (so a combination of alterations). We see in Fig. 21 that different ratios and doses of denosumab and romosozumab would have to be used to achieve the different therapies depending on the type of osteoporosis and the severity of the disease (which then should be carefully evaluated). We notice from these graphs that the appropriate ratio of denosumab and romosozumab is more sensitive to the type of disease rather than on the severity of the disease. We notice also that the ratio of drugs depends on the type of therapy being performed, except for senile osteoporosis, for which the ratio is pretty much constant around 35 whatever the type of therapy. However, the total dose varies with the type of therapy, as well as with the type of disease. As expected, the total dose required in the combination increases with the severity of the disease. But what is interesting is that the total dose seems to vary linearly with disease severity, with a similar linear coefficient for all disease types, and independently of the type of therapy, as seen in Fig. 21-b.

6 Model Assessment and Validation

In this section, we would like to propose a critical look at the model by summarizing our analysis on the assessment and validation of the model.

The model presented in Sects. 2 and 3 is derived from knowledge in the literature and is set up to be entirely mechanistic, perhaps with the exception of the dose-dependency of κ_2 in Eq. (42), where we used an exponential function to represent the saturation in the degradation of $\alpha S \circ S$. The mathematical formalism is well-grounded

as it is based on differential equations to represent time variations of cell densities. Cell signaling is carried out by cytokine secretion and cell responses are initiated and transduced from membrane-bound receptor occupancy. Law of mass action is assumed to represent the receptor/ligand binding kinetics. As explained in Sect. 2.3, the model is calibrated to behave similarly as what is observed in the literature, based on 43 qualitative checks. The model is also calibrated to match available quantitative data, such as appropriate range of cell densities, appropriate time scale of cell dynamics, and PK data of denosumab, romosozumab and PTH (1–34). As a result, the model is able to generate opposite outcomes from different dosing regimens of PTH, leading to either bone resorption, if PTH is administered continuously, or to bone formation, if PTH is administered in a pulsatory manner, as it is observed in clinical studies (Gogakos et al. 2009). This finding indicates that the differential action of PTH on the bone mass is a consequence of the difference in activation kinetics of the RANK-RANKL-OPG pathway and the Wnt-SOST pathway by PTH, which is a new result.

The model also provides excellent goodness-of-fit of PK concentration profiles of denosumab and romosozumab at different doses (Figs. 11 and 13). For example, the model captures well the nonlinearity in dose of both antibodies. As explained in Sects. 3.2 and 3.3, the PK models for denosumab and romosozumab are interrelated with the biological model (the bone model) through L for denosumab, and through π_P and κ_1 for romosozumab. Moreover, the bone model was calibrated first and independently of the PK models. So if the bone model was generating wrong estimates of bone cell densities and other bone-related quantities, it might not be possible to achieve a good fit with the PK models, since the PK model is dependent on the biological model. In these conditions, the excellent goodness-of-fit of the PK data could be considered as a validation of both the PK models and the biological model. We think that the higher mechanistic degree brought by the biological model enhances the goodness-of-fit of the PK models.

Most of the model parameters cannot be directly measured experimentally, or hardly, because they represent biological or biochemical processes which were combined together in the making of the model. However, there are some model parameters for which we can find experimental estimates in the literature. As explained in Sect. 2.3, the model parameters in Table 2 were all estimated at once using sophisticated optimization algorithms, based on diverse information and data from the literature. That is a completely different approach than measuring every single parameter individually by running a series of experiments. So comparing model-derived parameter values with experimentally determined values has to be done with care, by making sure for example, that they represent the same thing, or by being well aware of their difference. Nonetheless, if a number of model-derived parameters have comparable values with values measured experimentally, it is in general a good indication that the model is well-grounded and properly calibrated, and this could be considered as additional model validation elements. For example, the dissociation coefficient of the RANK-RANKL binding is represented in the model by $k_D^L = \frac{k_4}{k_3}$. The value found from parameter estimation is 178 pM. We found in the literature that this parameter has been measured by Biacore at about 100 pM, which is quite similar (Liu et al. 2010; Zhang et al. 2009). In our PK models, we computed the volume of distribution of hPTH(1–34) (teriparatide) at about 9 L. This is also what is found in the literature

for 75 kg individuals (Tang et al. 2004). We computed the volume of distribution of denosumab at about 4 L, and the rate of absorption from a subcutaneous site at about 0.77 day^{-1}. Reported values in the literature are about 3 L for the volume of distribution in 75 kg patients, and about 0.21 day^{-1} for the absorption rate, which are both relatively similar to what we found using different approaches (Sutjandra et al. 2011). Finally, we computed the bioavailability of romosozumab after subcutaneous injection at 69%. Reported values indicate a range from 50 to 70% (Paton 2014).

The model exhibits a number of non-obvious behaviors, which have been observed in the real system (known behaviors), but which were not used to calibrate the model in any way. These de novo behaviors can then be considered as post hoc validation of the model. For example, the two smallest doses after subcutaneous injection in the romosozumab study by Padhi et al. have almost no effect on bone turnover biomarkers, the third smallest dose has limited but measurable effect, and the remaining three largest doses have significant effects on the bone turnover biomarkers in a dose–response fashion (Padhi et al. 2011). This is exactly what we observed in the model with bone cells changes after subcutaneous administration of same romosozumab doses (see Fig. 15), whereas no relation between romosozumab doses and the magnitude in bone cells changes was used during model calibration. Similarly, 80% reduction in bone turnover biomarkers after subcutaneous injection of 60 mg denosumab was observed (Block et al. 2012). We also observe about 80% reduction in bone cells after injection of 65 mg denosumab (see Fig. 14-c). In another paper, it is observed from 50 to 90% reduction in bone turnover biomarkers in a dose–response fashion after subcutaneous injection of 0.3, 1 and 3 mg/kg denosumab (Kumagai et al. 2011). Again, we observe a similar reduction in bone cells at same doses (see Fig. 14b–d). This quantitative adequacy is striking considering that no relation between denosumab dose and response was used in the model calibration.

We have seen in Sect. 5 that the model can be used to simulate categories of osteoporosis, producing bone turnover values, in the disease states, very similar to what is seen in patients, in postmenopausal osteoporosis, senile osteoporosis and glucocorticoid-induced osteoporosis. Yet, no information or data about these diseases were used to calibrate the model. For example, simulation of senile osteoporosis shows an apparent uncoupling between osteoblasts and osteoclasts that is also seen in patients (Vasikaran 2008). So again these findings should be considered as post hoc validation of the model.

We mentioned in the introduction that bone remodeling is a localized process that can be modulated by systemic factors, such as estrogen, PTH, vitamin D, calcium homeostasis, as well as mechanical inputs. Some of these factors are not fully described in the model. We assume that the systemic factors that are not represented in the model are considered averaged over a population of individuals. However, if a question would involve a change over time of any of these systemic factors, the model may not be directly applicable to answer that question. For example, if a question would relate to the change in calcium level after administration of denosumab, or would be to determine the change in bone cells number after a calcium rich diet, the model, as it is, might not be directly applicable. For this particular question, physiology of the gut, kidney, parathyroid gland, and a representation of the calcium homeostasis, in relation to bone biology, would need to be added to the model (Peterson and Riggs 2010).

7 Conclusion

In this paper, we proposed a mathematical model describing the dynamics of bone cell signaling based on a previously published model (Lemaire et al. 2004). This earlier model has been used by many authors, which substantiates the need of such modeling framework (Ayati et al. 2010; Berkhout et al. 2015; Komarova 2005; Marathe et al. 2008, 2011; Peterson and Riggs 2010, 2012; Pivonka and Komarova 2010; Pivonka et al. 2008, 2010; Post et al. 2010, 2013; Ryser et al. 2009; Schmidt et al. 2011; Zumsande et al. 2011). The current model has been extended to include the effect of the Wnt molecules on the osteoblast lineage and the inhibition of that pathway by sclerostin (the SOST protein). Other recent models of bone remodeling have also included a representation of the Wnt/SOST pathway; however, they were developed to tackle different questions (Eudy et al. 2015; Graham et al. 2013). The model equations have been almost entirely reworked and simplified from the initial model. The model has then been completely recalibrated using 57 checks from the literature. Specific optimization methods based on qualitative objectives have been developed to perform the model calibration. We also incorporated PK layers of three drugs to the model, teriparatide (a fragment of human PTH), denosumab (a RANKL antibody), and romosozumab (a sclerostin antibody). These PK models are connected to the biological model so the PK of the drugs depend, to some extent, on the dynamics of the bone cells. The PK models were calibrated separately using PK clinical data from the literature. The goodness-of-fit of the PK models is excellent, and we think the fit is improved by the mechanistic nature of the biological model. The model successfully reproduces all 57 literature checks mentioned above, which comprises a lot of what is known about the dynamics of bone cells, including values of bone cell densities under "normal" conditions, typical time frame of bone remodeling, the tight coupling between osteoblasts and osteoclasts, the anabolic action of OPG, the catabolic action of RANKL. The model is also able to generate different bone cells responses in function of different modes of administration of PTH. Indeed, similarly to what has been observed in the clinics, the model leads to bone formation if PTH is injected daily but causes bone loss from chronic hyperparathyroidism, due to sustained over-production of PTH. The fact that the model can reproduce the paradoxical effect of PTH without added mechanisms provides an explanation of that effect, which has been elusive for long. Our findings indicate that the differential action of PTH on the bone mass might just be a consequence of the difference in activation kinetics of the RANK-RANKL-OPG pathway and the Wnt-SOST pathway by PTH. We used the model to simulate different categories of osteoporosis, namely postmenopausal osteoporosis, senile osteoporosis, glucocorticoid-induced osteoporosis, hyperparathyroidism and vitamin D deficiency. The main attributes of each disease are well captured by the model, for example bone turnover in the disease state. We used the model to compute adequate treatments for each disease composed of a combination of denosumab and romosozumab. We were able to identify appropriate ratio and total dose of both drugs in function of the category of osteoporosis and degree of severity of the disease. These doses and ratios are based on human clinical data (used in model calibration) so they may be used for exploring and informing what could be anticipated during treatment with these drugs, at least qualitatively. The model also indicates that these ratios and doses are highly dependent

on the disease type, the disease severity, the therapy type, the timing of therapy start, and other factors that may be different from patient to patient. We thus anticipate that the ratios and doses provided by the model will be different in different patient.

We hope that this model provides a basis for bone remodeling and bone cell signaling modeling, and could be used for many other applications than those we have shown in this paper. For example, something we have not done in this paper but would be worth doing would be to simulate bone diseases, as we did in Sect. 4, and do a full scan of the model parameters to identify novel targets (or combination of targets) for therapeutic interventions. This was done in our initial paper (Lemaire et al. 2004), as well as by other authors (Pivonka et al. 2010). Or we could do the same thing to identify potential biomarkers of response after a treatment. For known biomarkers, biomarker layers could be added, the way we added PK layers. This was done by several authors who included representations of resorption biomarkers such as NTx or CTx, or bone mineral density (BMD) (Marathe et al. 2011; Peterson and Riggs 2012). More PK layers of other drugs could also easily be added and tested, without recalibrating the bone model. And virtual clinical trials could be ran for healthy subjects or osteoporosis patients by incorporating patient's variability in the model parameters. This model could also be used to test or explore other therapeutic entities, such as bispecific antibodies. It could also be used for osteoporosis patients with impaired physiological functions (Riggs et al. 2012), or even for completely different indications, such as multiple myeloma (Marathe et al. 2008; Wang and Lin 2012). Of course, this model can always be complexified as new understanding of the biology emerges, as we did by incorporating the Wnt-SOST pathway. Finally, as the model describes the core regulation of osteoblasts and osteoclasts at the level of the bone microenvironment, it is rather modular in nature and can be combined with other models to describe wider systems (Peterson and Riggs 2010).

Acknowledgements VL would like to thank Donna Stone, Kris Poulsen, Arvind Rajpal and Dave Shelton for fruitful discussions during the realization of this study.

References

Allen RJ, Rieger TR, Musante CJ (2016) Efficient generation and selection of virtual populations in quantitative systems pharmacology models. CPT Pharmacomet Syst Pharmacol 5:140–146. https://doi.org/10.1002/psp4.12063

Aloia JF, Feuerman M, Yeh JK (2006) Reference range for serum parathyroid hormone. Endocr Pract 12:137–144. https://doi.org/10.4158/EP.12.2.137

Amgen (2009) Romosozumab nonproprietary drug name

Amgen (2010) Prolia® (denosumab)

Ayati BP, Edwards CM, Webb GF, Wikswo JP (2010) A mathematical model of bone remodeling dynamics for normal bone cell populations and myeloma bone disease. Biol Direct 5:28. https://doi.org/10.1186/1745-6150-5-28

Bekker PJ, Holloway DL, Rasmussen AS, Murphy R, Martin SW, Leese PT, Holmes GB, Dunstan CR, DePaoli AM (2004) A single-dose placebo-controlled study of AMG 162, a fully human monoclonal antibody to RANKL, in postmenopausal women. J Bone Miner Res 19:1059–1066. https://doi.org/10.1359/JBMR.040305

Bellido T, Ali AA, Plotkin LI, Fu Q, Gubrij I, Roberson PK, Weinstein RS, O'Brien CA, Manolagas SC, Jilka RL (2003) Proteasomal degradation of Runx2 shortens parathyroid hormone-induced anti-apoptotic

signaling in osteoblasts A putative explanation for why intermittent administration is needed for bone anabolism. J Biol Chem 278:50259–50272
Bellido T, Ali A, Gubrij I, Plotkin L, Fu Q, O'brien C, Manolagas S, Jilka R (2005) Chronic elevation of parathyroid hormone in mice reduces expression of sclerostin by osteocytes: a novel mechanism for hormonal control of osteoblastogenesis. Endocrinology 146:4577–4583
Bergwitz C, Jüppner H (2010) Regulation of phosphate homeostasis by PTH, vitamin D, and FGF23. Annu Rev Med 61:91–104. https://doi.org/10.1146/annurev.med.051308.111339
Berkhout J, Stone JA, Verhamme KM, Stricker BH, Sturkenboom MC, Danhof M, Post TM (2015) Application of a systems pharmacology-based placebo population model to analyze long-term data of postmenopausal osteoporosis. CPT Pharmacomet Syst Pharmacol 4:516–526. https://doi.org/10.1002/psp4.12006
Block GA, Bone HG, Fang L, Lee E, Padhi D (2012) A single-dose study of denosumab in patients with various degrees of renal impairment. J Bone Miner Res 27:1471–1479. https://doi.org/10.1002/jbmr.1613
Bone HG, Bolognese MA, Yuen CK, Kendler DL, Wang H, Liu Y, San Martin J (2008) Effects of denosumab on bone mineral density and bone turnover in postmenopausal women. J Clin Endocrinol Metab 93:2149–2157. https://doi.org/10.1210/jc.2007-2814
Bone HG, Bolognese MA, Yuen CK, Kendler DL, Miller PD, Yang Y-C, Grazette L, San Martin J, Gallagher JC (2011) Effects of denosumab treatment and discontinuation on bone mineral density and bone turnover markers in postmenopausal women with low bone mass. J Clin Endocrinol Metab 96:972–980. https://doi.org/10.1210/jc.2010-1502
Bonewald LF, Johnson ML (2008) Osteocytes, mechanosensing and Wnt signaling. Bone 42:606–615
Canalis E, Giustina A, Bilezikian JP (2007a) Mechanisms of anabolic therapies for osteoporosis. N Engl J Med 357:905–916. https://doi.org/10.1056/NEJMra067395
Canalis E, Mazziotti G, Giustina A, Bilezikian J (2007b) Glucocorticoid-induced osteoporosis: pathophysiology and therapy. Osteoporos Int 18:1319–1328
Cho C, Greller L, Tobin F (2000) Parathyroid hormone receptor and osteoporosis—towards target validation by mathematical modeling. Bioinform Math Biol Bone Cartil Biol—SmithKline Beecham Pharmaceuticals R&D, King of Prussia, PA, USA
Chu NN, Li XN, Chen WL, Xu HR (2007) Pharmacokinetics and safety of recombinant human parathyroid hormone (1–34) (teriparatide) after single ascending doses in Chinese healthy volunteers. Pharmazie 62:869–871
Clausen JO (2009) Comment on Kanis et al.: "European guidance for the diagnosis and management of osteoporosis in postmenopausal women". Osteoporos Int 20:1631. https://doi.org/10.1007/s00198-008-0812-y
Daddona PE, Matriano JA, Mandema J, Maa YF (2011) Parathyroid hormone (1–34)-coated microneedle patch system: clinical pharmacokinetics and pharmacodynamics for treatment of osteoporosis. Pharm Res 28:159–165. https://doi.org/10.1007/s11095-010-0192-9
Daoussis D, Andonopoulos AP (2011) The emerging role of Dickkopf-1 in bone biology: is it the main switch controlling bone and joint remodeling? Semin Arthritis Rheum 41:170–177. https://doi.org/10.1016/j.semarthrit.2011.01.006
Ellies DL, Viviano B, McCarthy J, Rey JP, Itasaki N, Saunders S, Krumlauf R (2006) Bone density ligand, Sclerostin, directly interacts with LRP5 but not LRP5G171 V to modulate Wnt activity. J Bone Miner Res 21:1738–1749
Eudy RJ, Gastonguay MR, Baron KT, Riggs MM (2015) Connecting the dots: linking osteocyte activity and therapeutic modulation of sclerostin by extending a multiscale systems model. CPT Pharmacomet Syst Pharmacol 4:527–536. https://doi.org/10.1002/psp4.12013
Fermor B, Skerry TM (1995) PTH/PTHrP receptor expression on osteoblasts and osteocytes but not resorbing bone surfaces in growing rats. J Bone Miner Res 10:1935–1943
Fraher LJ, Klein K, Marier R, Freeman D, Hendy GN, Goltzman D, Hodsman AB (1995) Comparison of the pharmacokinetics of parenteral parathyroid hormone-(1–34) [PTH-(1–34)] and PTH-related peptide-(1–34) in healthy young humans. J Clin Endocrinol Metab 80:60–64
Fromigue O, Modrowski D, Marie PJ (2004) Growth factors and bone formation in osteoporosis: roles for fibroblast growth factor and transforming growth factor beta. Curr Pharm Des 10:2593–2603
Furuya M, Kikuta J, Fujimori S, Seno S, Maeda H, Shirazaki M, Uenaka M, Mizuno H, Iwamoto Y, Morimoto A, Hashimoto K, Ito T, Isogai Y, Kashii M, Kaito T, Ohba S, Chung UI, Lichtler AC, Kikuchi K, Matsuda H, Yoshikawa H, Ishii M (2018) Direct cell-cell contact between mature osteoblasts and

osteoclasts dynamically controls their functions in vivo. Nat Commun 9:300. https://doi.org/10.1038/s41467-017-02541-w
Gadkar K, Budha N, Baruch A, Davis JD, Fielder P, Ramanujan S (2014) A mechanistic systems pharmacology model for prediction of LDL cholesterol lowering by PCSK9 antagonism in human dyslipidemic populations. CPT Pharmacomet Syst Pharmacol 3:e149. https://doi.org/10.1038/psp.2014.47
Gibiansky L, Sutjandra L, Doshi S, Zheng J, Sohn W, Peterson MC, Jang GR, Chow AT, Perez-Ruixo JJ (2012) Population pharmacokinetic analysis of denosumab in patients with bone metastases from solid tumours. Clin Pharmacokinet 51:247–260. https://doi.org/10.2165/11598090-000000000-00000
Gogakos AI, Cheung MS, Bassett JD, Williams GR (2009) Bone signaling pathways and treatment of osteoporosis. Expert Rev Endocrinol Metab 4:639–650
Goldring SR, Goldring MB (2007) Eating bone or adding it: the Wnt pathway decides. Nat Med 13:133–134
Graham JM, Ayati BP, Holstein SA, Martin JA (2013) The role of osteocytes in targeted bone remodeling: a mathematical model. PLoS ONE 8:e63884. https://doi.org/10.1371/journal.pone.0063884
Hammerle SP, Mindeholm L, Launonen A, Kiese B, Loeffler R, Harfst E, Azria M, Arnold M, John MR (2012) The single dose pharmacokinetic profile of a novel oral human parathyroid hormone formulation in healthy postmenopausal women. Bone 50:965–973. https://doi.org/10.1016/j.bone.2012.01.009
Holick MF (2007) Vitamin D deficiency. N Engl J Med 357:266–281. https://doi.org/10.1056/NEJMra070553
Ishibashi Y, Yoshida H, Mizuta E, Fukuda T (1993) Fragmentation of parathyroid hormone, a 9.4 kDa polypeptide, in liquid secondary ion mass spectrometry. Biol Mass Spectrom 22:98–100. https://doi.org/10.1002/bms.1200220113
Jabbar S, Drury J, Fordham JN, Datta HK, Francis RM, Tuck SP (2011) Osteoprotegerin, RANKL and bone turnover in postmenopausal osteoporosis. J Clin Pathol 64:354–357
Jilka RL (2007) Molecular and cellular mechanisms of the anabolic effect of intermittent PTH. Bone 40:1434–1446
Kassem M, Marie PJ (2011) Senescence-associated intrinsic mechanisms of osteoblast dysfunctions. Aging Cell 10:191–197. https://doi.org/10.1111/j.1474-9726.2011.00669.x
Keller H, Kneissel M (2005) SOST is a target gene for PTH in bone. Bone 37:148–158
Kendler DL, Roux C, Benhamou CL, Brown JP, Lillestol M, Siddhanti S, Man H-S, Martin JS, Bone HG (2010) Effects of denosumab on bone mineral density and bone turnover in postmenopausal women transitioning from alendronate therapy. J Bone Miner Res 25:72–81. https://doi.org/10.1359/jbmr.090716
Khosla S, Westendorf JJ, Oursler MJ (2008) Building bone to reverse osteoporosis and repair fractures. J Clin Invest 118:421–428. https://doi.org/10.1172/JCI33612
Komarova SV (2005) Mathematical model of paracrine interactions between osteoclasts and osteoblasts predicts anabolic action of parathyroid hormone on bone. Endocrinology 146:3589–3595
Kramer I, Halleux C, Keller H, Pegurri M, Gooi JH, Weber PB, Feng JQ, Bonewald LF, Kneissel M (2010) Osteocyte Wnt/beta-catenin signaling is required for normal bone homeostasis. Mol Cell Biol 30:3071–3085. https://doi.org/10.1128/MCB.01428-09
Kumagai Y, Hasunuma T, Padhi D (2011) A randomized, double-blind, placebo-controlled, single-dose study to evaluate the safety, tolerability, pharmacokinetics and pharmacodynamics of denosumab administered subcutaneously to postmenopausal Japanese women. Bone 49:1101–1107. https://doi.org/10.1016/j.bone.2011.08.007
Lacey DL, Boyle WJ, Simonet WS, Kostenuik PJ, Dougall WC, Sullivan JK, San Martin J, Dansey R (2012) Bench to bedside: elucidation of the OPG-RANK-RANKL pathway and the development of denosumab. Nat Rev Drug Discov 11:401–419. https://doi.org/10.1038/nrd3705
Lemaire V, Tobin FL, Greller LD, Cho CR, Suva LJ (2004) Modeling the interactions between osteoblast and osteoclast activities in bone remodeling. J Theor Biol 229:293–309. https://doi.org/10.1016/j.jtbi.2004.03.023
Lewiecki EM (2011) Sclerostin monoclonal antibody therapy with AMG 785: a potential treatment for osteoporosis. Expert Opin Biol Ther 11:117–127
Li X, Zhang Y, Kang H, Liu W, Liu P, Zhang J, Harris SE, Wu D (2005) Sclerostin binds to LRP5/6 and antagonizes canonical Wnt signaling. J Biol Chem 280:19883–19887
Li X, Ominsky MS, Warmington KS, Morony S, Gong J, Cao J, Gao Y, Shalhoub V, Tipton B, Haldankar R, Chen Q, Winters A, Boone T, Geng Z, Niu QT, Ke HZ, Kostenuik PJ, Simonet WS, Lacey DL, Paszty C (2009) Sclerostin antibody treatment increases bone formation, bone mass, and bone strength in a

rat model of postmenopausal osteoporosis. J Bone Miner Res 24:578–588. https://doi.org/10.1359/jbmr.081206
Lindsay R, Nieves J, Henneman E, Shen V, Cosman F (1993) Subcutaneous administration of the amino-terminal fragment of human parathyroid hormone-(1–34): kinetics and biochemical response in estrogenized osteoporotic patients. J Clin Endocrinol Metab 77:1535–1539
Liu C, Walter TS, Huang P, Zhang S, Zhu X, Wu Y, Wedderburn LR, Tang P, Owens RJ, Stuart DI (2010) Structural and functional insights of RANKL–RANK interaction and signaling. J Immunol 184:6910–6919
Lorentzon M, Cummings SR (2015) Osteoporosis: the evolution of a diagnosis. J Intern Med 277:650–661. https://doi.org/10.1111/joim.12369
Marathe A, Peterson MC, Mager DE (2008) Integrated cellular bone homeostasis model for denosumab pharmacodynamics in multiple myeloma patients. J Pharmacol Exp Ther 326:555–562
Marathe DD, Marathe A, Mager DE (2011) Integrated model for denosumab and ibandronate pharmacodynamics in postmenopausal women. Biopharm Drug Dispos 32:471–481
Mazziotti G, Angeli A, Bilezikian JP, Canalis E, Giustina A (2006) Glucocorticoid-induced osteoporosis: an update. Trends Endocrinol Metab 17:144–149. https://doi.org/10.1016/j.tem.2006.03.009
Moerman EJ, Teng K, Lipschitz DA, Lecka-Czernik B (2004) Aging activates adipogenic and suppresses osteogenic programs in mesenchymal marrow stroma/stem cells: the role of PPAR-γ2 transcription factor and TGF-β/BMP signaling pathways. Aging Cell 3:379–389. https://doi.org/10.1111/j.1474-9728.2004.00127.x
Mosekilde L (2008) Primary hyperparathyroidism and the skeleton. Clin Endocrinol 69:1–19
O'Brien CA, Jia D, Plotkin LI, Bellido T, Powers CC, Stewart SA, Manolagas SC, Weinstein RS (2004) Glucocorticoids act directly on osteoblasts and osteocytes to induce their apoptosis and reduce bone formation and strength. Endocrinology 145:1835–1841. https://doi.org/10.1210/en.2003-0990
Padhi D, Jang G, Stouch B, Fang L, Posvar E (2011) Single-dose, placebo-controlled, randomized study of AMG 785, a sclerostin monoclonal antibody. J Bone Miner Res 26:19–26. https://doi.org/10.1002/jbmr.173
Paszty C, Turner CH, Robinson MK (2010) Sclerostin: a gem from the genome leads to bone-building antibodies. J Bone Miner Res 25:1897–1904. https://doi.org/10.1002/jbmr.161
Paton DM (2014) Romosozumab. Humanized anti-sclerostin monoclonal antibody, treatment of osteoporosis. Drugs of the Future, 553–556
Peterson MC, Riggs MM (2010) A physiologically based mathematical model of integrated calcium homeostasis and bone remodeling. Bone 46:49–63. https://doi.org/10.1016/j.bone.2009.08.053
Peterson M, Riggs M (2012) Predicting nonlinear changes in bone mineral density over time using a multiscale systems pharmacology model. CPT: Pharmacomet Syst Pharmacol 1:1–8. https://doi.org/10.1038/psp.2012.15
Pfutzner A, Flacke F, Pohl R, Linkie D, Engelbach M, Woods R, Forst T, Beyer J, Steiner SS (2003) Pilot study with technosphere/PTH(1–34)–a new approach for effective pulmonary delivery of parathyroid hormone (1–34). Horm Metab Res 35:319–323. https://doi.org/10.1055/s-2003-41309
Pietschmann P, Rauner M, Sipos W, Kerschan-Schindl K (2009) Osteoporosis: an age-related and gender-specific disease-a mini-review. Gerontology 55:3
Pivonka P, Komarova SV (2010) Mathematical modeling in bone biology: from intracellular signaling to tissue mechanics. Bone 47:181–189. https://doi.org/10.1016/j.bone.2010.04.601
Pivonka P, Zimak J, Smith DW, Gardiner BS, Dunstan CR, Sims NA, Martin TJ, Mundy GR (2008) Model structure and control of bone remodeling: a theoretical study. Bone 43:249–263. https://doi.org/10.1016/j.bone.2008.03.025
Pivonka P, Zimak J, Smith DW, Gardiner BS, Dunstan CR, Sims NA, Martin TJ, Mundy GR (2010) Theoretical investigation of the role of the RANK-RANKL-OPG system in bone remodeling. J Theor Biol 262:306–316. https://doi.org/10.1016/j.jtbi.2009.09.021
Post TM, Cremers SC, Kerbusch T, Danhof M (2010) Bone physiology, disease and treatment: towards disease system analysis in osteoporosis. Clin Pharmacokinet 49:89–118. https://doi.org/10.2165/11318150-000000000-00000
Post TM, Schmidt S, Peletier LA, de Greef R, Kerbusch T, Danhof M (2013) Application of a mechanism-based disease systems model for osteoporosis to clinical data. J Pharmacokinet Pharmacodyn 40:143–156. https://doi.org/10.1007/s10928-012-9294-9

Potter LK, Greller LD, Cho CR, Nuttall ME, Stroup GB, Suva LJ, Tobin FL (2005) Response to continuous and pulsatile PTH dosing: a mathematical model for parathyroid hormone receptor kinetics. Bone 37:159–169

Riggs MM, Peterson MC, Gastonguay MR (2012) Multiscale physiology-based modeling of mineral bone disorder in patients with impaired kidney function. J Clin Pharmacol 52:45S–53S

Ross DS, Battista C, Cabal A, Mehta K (2012) Dynamics of bone cell signaling and PTH treatments of osteoporosis. Discrete Contin Dyn Syst Ser B 17:2185–2200. https://doi.org/10.3934/dcdsb.2012.17.2185

Ryser MD, Nigam N, Komarova SV (2009) Mathematical modeling of spatio-temporal dynamics of a single bone multicellular unit. J Bone Miner Res 24:860–870. https://doi.org/10.1359/jbmr.081229

Scheiner S, Pivonka P, Smith DW, Dunstan CR, Hellmich C (2014) Mathematical modeling of postmenopausal osteoporosis and its treatment by the anti-catabolic drug denosumab. Int J Numer Method Biomed Eng 30:1–27. https://doi.org/10.1002/cnm.2584

Schmidt S, Post TM, Peletier LA, Boroujerdi MA, Danhof M (2011) Coping with time scales in disease systems analysis: application to bone remodeling. J Pharmacokinet Pharmacodyn 38:873–900. https://doi.org/10.1007/s10928-011-9224-2

Sigma-Aldrich (2008) Parathyroid hormone fragment 1-34 human. Sigma-Aldrich

Sipos W, Pietschmann P, Rauner M, Kerschan-Schindl K, Patsch J (2009) Pathophysiology of osteoporosis. Wien Med Wochenschr 159:230–234. https://doi.org/10.1007/s10354-009-0647-y

Sutjandra L, Rodriguez RD, Doshi S, Ma M, Peterson MC, Jang GR, Chow AT, Perez-Ruixo JJ (2011) Population pharmacokinetic meta-analysis of denosumab in healthy subjects and postmenopausal women with osteopenia or osteoporosis. Clin Pharmacokinet 50:793–807. https://doi.org/10.2165/11594240-000000000-00000

Tang L, Persky AM, Hochhaus G, Meibohm B (2004) Pharmacokinetic aspects of biotechnology products. J Pharm Sci 93:2184–2204

Vacanti C, Pietrzak WS (2008) Musculoskeletal tissue regeneration: biological materials and methods. Springer, Berlin

Vasikaran SD (2008) Utility of biochemical markers of bone turnover and bone mineral density in management of osteoporosis. Crit Rev Clin Lab Sci 45:221–258. https://doi.org/10.1080/10408360801949442

Wang Y, Lin B (2012) In silico investigations of the anti-catabolic effects of pamidronate and denosumab on multiple myeloma-induced bone disease

Wang Y, Pivonka P, Buenzli PR, Smith DW, Dunstan CR (2011) Computational modeling of interactions between multiple myeloma and the bone microenvironment. PLoS ONE 6:e27494. https://doi.org/10.1371/journal.pone.0027494

Weinstein R (2001) Glucocorticoid-induced osteoporosis. Rev Endocr Metab Disord 2:65–73. https://doi.org/10.1023/A:1010007108155

Yonemori K, Fujiwara Y, Minami H, Kitagawa K, Fujii H, Arai T, Sohn W, Ohkura M, Ohtsu T (2008) Phase 1 trial of denosumab safety, pharmacokinetics, and pharmacodynamics in Japanese women with breast cancer-related bone metastases. Cancer Sci 99:1237–1242. https://doi.org/10.1111/j.1349-7006.2008.00803.x

Zhang S, Liu C, Huang P, Zhou S, Ren J, Kitamura Y, Tang P, Bi Z, Gao B (2009) The affinity of human RANK binding to its ligand RANKL. Arch Biochem Biophys 487:49–53

Zumsande M, Stiefs D, Siegmund S, Gross T (2011) General analysis of mathematical models for bone remodeling. Bone 48:910–917. https://doi.org/10.1016/j.bone.2010.12.010

Affiliations

Vincent Lemaire[1,2] · David R. Cox[1]

✉ Vincent Lemaire
vincent514@gmail.com; lemaire.vincent@gene.com

1 Rinat (Pfizer Inc.), 230 East Grand Avenue, South San Francisco, CA 94080, USA

2 Present Address: Genentech, 1 DNA Way, MS 463A, South San Francisco, CA 94080, USA